AIMS Mathematics, 11(6): 15402–15434.
DOI: 10.3934/math.2026633
Received: 02 March 2026
Revised: 08 May 2026
Accepted: 12 May 2026
Published: 01 June 2026

http://www.aimspress.com/journal/Math

Research article

A comparative analysis of dynamics in the generalized Lorenz model with feedforward neural network validation

Ahmed Omar Alzahrani[1], Israr Ahmad[2,*], Ahmed Mohammed Alghamdi[3,*], Adel Aboud Bahaddad[4] and Khalid Ali Almarhabi[5]

[1] Department of Information Systems and Technology, College of Computer Science and Engineering, University of Jeddah, Jeddah 21493, Saudi Arabia

[2] Department of Mathematics, Government Post Graduate Jahanzeb College, Swat 19130, Khyber Pakhtunkhwa, Pakistan

[3] Department of Software Engineering, College of Computer Science and Engineering, University of Jeddah, Jeddah 21493, Saudi Arabia

[4] Department of Information System, Faculty of Computing and Information Technology, King Abdulaziz University, Jeddah 21589, Saudi Arabia

[5] Department of Computer Science, College of Engineering and Computing in Al-Qunfudah, Umm Al-Qura University, Makkah 24381, Saudi Arabia

* **Correspondence:** Email: israrahmad@jc.edu.pk, amalghamdi@uj.edu.sa.

Abstract: This paper presents a comprehensive analysis of the Lorenz model under the generalized ψ-Hilfer fractional derivative, which offers remarkable flexibility through its fractional order θ, type parameter κ, and auxiliary function $\psi(t)$. The primary contributions of this work are threefold: First, we provided a detailed qualitative study establishing the existence, uniqueness, and Ulam-Hyers stability using fixed point theory. Second, we developed a novel hybrid numerical scheme specifically designed for the ψ-Hilfer fractional Lorenz system. Third, we validated the numerical solutions using a feedforward neural network trained on numerically generated data, providing independent verification of our results. Quantitative performance metrics confirmed excellent agreement between numerical solutions and neural network approximations, with mean squared error values ranging from 1.085 to 5.186 and R^2 values between 0.937 and 0.983 across all state variables. MATLAB simulations comprise two-dimensional and three-dimensional visualizations, which demonstrated how variations in the fractional order θ and type parameter κ significantly influence solution profiles, with decreasing fractional order enhancing memory effects and stabilizing system dynamics. Our work demonstrates how the additional flexibility of the ψ-Hilfer operator enables more accurate modeling of memory effects in chaotic systems, while neural network validation provides a robust framework for solution verification.

Keywords: Lorenz model; ψ-Hilfer derivative; hybrid numerical scheme; neural networks; chaotic dynamics
Mathematics Subject Classification: 03C65, 26A33, 34A08, 92B20

1. Introduction

The Lorenz system is one of the most extensively studied nonlinear dynamical systems in the theory of chaos and complex dynamics. Originally introduced as a simplified model of atmospheric convection, this three-dimensional system has since become a cornerstone of modern nonlinear science and a paradigmatic example of deterministic chaos [1]. The Lorenz system has wide applications in various scientific disciplines, including meteorology, fluid mechanics, nonlinear control theory, and chaos-based secure communication [2]. Beyond its meteorological origins, the system exhibits rich dynamical behavior, encompassing equilibrium points, periodic orbits, and chaotic attractors, which has made it an indispensable tool for investigating complex phenomena across physics, engineering, and biological systems [3].

The classical Lorenz system is expressed as

$$\begin{cases} \dfrac{d\mathrm{x}}{dt} = \sigma(\mathrm{y} - \mathrm{x}), \\ \dfrac{d\mathrm{y}}{dt} = \mathrm{x}(\rho - \mathrm{z}) - \mathrm{y}, \\ \dfrac{d\mathrm{z}}{dt} = \mathrm{xy} - \beta\mathrm{z}. \end{cases} \tag{1.1}$$

The variable $x(t)$ represents the intensity of convective motion, $y(t)$ describes the horizontal temperature variation, and $z(t)$ represents the vertical temperature distribution in the fluid layer. The parameters σ, ρ, and β are positive constants that characterize the physical properties of the system. Specifically, σ is associated with the Prandtl number, which measures the ratio of momentum diffusivity to thermal diffusivity; ρ is related to the Rayleigh number, controlling thermal forcing; and β is a geometric parameter depending on the aspect ratio of the fluid layer.

Fractional calculus is known for its memory and hereditary properties in different dynamical systems. Moreover, it gives a generalization to integer-order systems [4]. It is essential for the generalizations of the Lorenz system to accurately describe complex physical processes by incorporating memory effects and nonlocal dynamics [5]. The importance of the ψ-Hilfer derivative is clear from its extraordinary flexibility and versatility. This operator has the beautiful quality that it can, at one time, recover the Riemann-Liouville, Caputo, and Hadamard derivatives [6]. This derivative has two parameters, θ and κ, which are responsible for offering flexibility in the process of modeling [7]. Consequently, it can capture rich dynamical behaviors where other operators fall short. Another interesting feature in the mentioned derivative is the inclusion of the $\psi(t)$ function, which makes it totally different from other fractional derivatives. We can adjust this function as needed based on the analysis.

Recent advances in fractional calculus have witnessed significant contributions from various research groups. In [8], the authors have extensively explored fractional differential equations

using artificial intelligence techniques. Their studies on fractional-order systems have demonstrated the effectiveness of neural networks in approximating solutions of nonlinear fractional differential equations. In this direction, a series of subsequent contributions has been reported, including hybrid intelligent frameworks for fractional-order neuron models [9] and Bayesian regularization neural networks for magnetized nanofluid flows [10]. Additional contributions include Levenberg-Marquardt networks for Casson fluid dynamics [11] and neural network designs for two-phase nanofluid heat transfer [12]. Further work has also explored machine learning architectures for Sisko nanofluid boundary layer flow [13] and intelligent frameworks for biomedical thermal modeling in blood [14]. In [15], the Caputo fractional Lorenz system was studied, and chaos was reported for specific parameter ranges. In [16], active control synchronization was investigated using predictor-corrector methods. High-precision numerical schemes for fractional-order chaotic systems were developed in [17], while attractor radius and predictability via the fourth-order Runge-Kutta method were investigated in [18]. Further contributions include the existence and controllability analysis of multi-term fractional coupled systems with generalized Caputo-Fabrizio operators [19] and efficient numerical schemes for linear fractional differential systems with applications to diffusion problems [20].

The application of machine learning techniques has revolutionized the study of Lorenz system behavior. The difference time series peak complexity algorithm addressed synchronization diagnostics in coupled Lorenz systems using entropy measures [21], while hybrid quantum-classical approaches employed the variational quantum linear solver for numerical solutions of the Lorenz system [22]. Recurrent neural networks and long short-term memory networks have been successfully applied to fractional-order chaotic Lorenz systems [23]. Recent studies have demonstrated the potential of physics-informed neural networks for solving fractional differential equations [24]. For more information about neural networks and the Lorenz system, one can see [25,26], which reveal that these networks can learn meaningful representations of the chaotic attractor even on unseen phase space regions. Moreover, these works have shown how neural networks can be hybridized with numerical and analytical methods for complex dynamical systems [27, 28].

Despite the extensive work on fractional Lorenz models under Caputo and Riemann-Liouville operators, several significant gaps remain:

- The analysis of the Lorenz model under the generalized ψ-Hilfer fractional derivative remains unexplored.
- Validation of fractional Lorenz models through independent machine learning methods is largely absent from the literature.
- Comprehensive qualitative analysis including existence, uniqueness, and stability for the ψ-Hilfer formulation has not been established.
- A systematic comparison between different fractional operators applied to the Lorenz system is missing.

Motivated by these considerations, we generalize (1.1) by formulating the Lorenz model using the ψ-Hilfer fractional derivative:

$$\begin{cases} {}^{H}\mathrm{D}_{0^+}^{\theta,\kappa;\psi}\mathrm{x}(t) = \sigma(\mathrm{y}-\mathrm{x}), \\ {}^{H}\mathrm{D}_{0^+}^{\theta,\kappa;\psi}\mathrm{y}(t) = \mathrm{x}(\rho-\mathrm{z})-\mathrm{y}, \\ {}^{H}\mathrm{D}_{0^+}^{\theta,\kappa;\psi}\mathrm{z}(t) = \mathrm{xy}-\beta\mathrm{z}, \\ I_{0^+}^{(1-\theta)(1-\kappa);\psi}\mathrm{x}(0^+) = \mathrm{x}_0 \geq 0, \\ I_{0^+}^{(1-\theta)(1-\kappa);\psi}\mathrm{y}(0^+) = \mathrm{y}_0 \geq 0, \\ I_{0^+}^{(1-\theta)(1-\kappa);\psi}\mathrm{z}(0^+) = \mathrm{z}_0 \geq 0. \end{cases} \tag{1.2}$$

Here ${}^{H}\mathrm{D}_{0^+}^{\theta,\kappa;\psi}$ denotes the ψ-Hilfer derivative of fractional order $\theta \in (0,1)$ and fractal dimension $\kappa \in [0,1]$. The initial condition is prescribed in terms of the ψ-fractional integral $I_{0^+}^{(1-\theta)(1-\kappa);\psi}$. The main novelties and contributions of our work are sixfold. First, we incorporate the ψ-Hilfer fractional operator, which generalizes classical, Caputo, and Hadamard derivatives. Second, we provide a comprehensive qualitative study establishing the existence, uniqueness, and Ulam-Hyers stability using fixed point theory. Third, we develop a novel numerical scheme specifically designed for the ψ-Hilfer fractional Lorenz system. Fourth, we validate the numerical solutions using a feedforward neural network trained on numerically generated data, providing independent verification of our results. Fifth, we conduct a complete analysis of the influence of fractional parameters θ and κ on system dynamics, revealing how memory effects alter chaotic behavior. Sixth, we present a systematic quantitative comparison with existing literature on Lorenz systems, fractional operators, and machine learning approaches.

The remainder of this paper is organized as follows: Section 2 presents the mathematical preliminaries and theoretical analysis of Model (1.2), including existence and uniqueness results. Section 3 is devoted to Ulam-Hyers (UH) stability analysis. Section 4 provides detailed numerical analysis, including the development of the numerical scheme, simulation results, and convergence analysis. In Section 5, we focus on neural network approximation, including dataset generation, network architecture, training methodology, and error analysis. A comprehensive comparative study and discussion of the results are presented in Section 6. Finally, Section 7 summarizes the work and outlines future research directions.

2. Mathematical preliminaries and theoretical analysis

We develop the Banach space $\mathcal{X} = \mathcal{Y} \times \mathcal{Y} \times \mathcal{Y}$ such that $\mathcal{Y} = C[0,\, T]$ and the norm is defined as follows:

$$\|(\mathrm{x},\, \mathrm{y},\, \mathrm{z})\| = \max_{t\in J}\left\{ \left|(\mathrm{x}(t), \mathrm{y}(t), \mathrm{z}(t))\right| \right\}, \quad \text{where } J = [0, T].$$

Definition 2.1. *[29] Let $\theta > 0$ and J be finite or infinite on the real line $\mathbb{R}$. Furthermore, the function ψ is an increasing and positive monotone on $(0, T)$. The left Riemann–Liouville fractional integral of a function $u \in C[0, T]$ with respect to another function $\psi \in C[0, T]$ is given as follows:*

$$I_{0^+}^{\theta;\psi}u(t) = \int_0^t \frac{\psi'(\xi)(\psi(t)-\psi(\xi))^{\theta-1}u(\xi)}{\Gamma(\theta)}\, d\xi.$$

Definition 2.2. *[29] Let $\theta > 0$, J be finite or infinite on the real line, $u \in C[0,T]$, and $\psi \in C[0,T]$ be a positive, increasing monotone function. The derivative of $\psi(t)$ is not zero for all values of t in the interval J. The ψ-Hilfer left fractional derivative is defined in the following way:*

$$ {}^{H}\mathrm{D}_{0^+}^{\theta,\kappa;\psi} u(t) = I_{0^+}^{\kappa(1-\theta);\psi} \left(\frac{1}{\psi'(t)} \frac{d}{dt} \right) I_{0^+}^{(1-\kappa)(1-\theta);\psi} u(t). $$

2.1. Reformulation of the problem

The following functions are defined for the rest of the work.

$$ \begin{cases} \Pi_1(t, \mathrm{x}, \mathrm{y}, \mathrm{z}) = \sigma(\mathrm{y} - \mathrm{x}), \\ \Pi_2(t, \mathrm{x}, \mathrm{y}, \mathrm{z}) = \mathrm{x}(\rho - \mathrm{z}) - \mathrm{y}, \\ \Pi_3(t, \mathrm{x}, \mathrm{y}, \mathrm{z}) = \mathrm{xy} - \beta \mathrm{z}. \end{cases} \tag{2.1} $$

$$ \begin{cases} \mathcal{G}(t) = (\mathrm{x}(t),\ \mathrm{y}(t),\ \mathrm{z}(t)), \\ \mathcal{G}(0) = (\mathrm{x}(0),\ \mathrm{y}(0),\ \mathrm{z}(0)), \\ \Pi(t, \mathcal{G}(t)) = (\Pi_1(t, \mathrm{x}, \mathrm{y}, \mathrm{z}),\ \Pi_2(t, \mathrm{x}, \mathrm{y}, \mathrm{z}),\ \Pi_3(t, \mathrm{x}, \mathrm{y}, \mathrm{z})). \end{cases} $$

Therefore Model (1.2) may obtain the following form:

$$ \begin{cases} {}^{H}\mathbb{D}_{0^+}^{\theta,\kappa;\psi} \mathcal{G}(t) = \Pi(t, \mathcal{G}(t)), \\ I_{0^+}^{(1-\theta)(1-\kappa);\psi} \mathcal{G}(0^+) = \mathcal{G}_0. \end{cases} \tag{2.2} $$

Lemma 2.3. *The solution of problem* (2.2) *obtains the following form:*

$$ \mathcal{G}(t) = \frac{\mathcal{G}_0}{\Gamma(\nu)} (\psi(t) - \psi(0))^{\nu-1} + \int_0^t \frac{\psi'(\xi)(\psi(t) - \psi(\xi))^{\theta-1} \Pi(\xi, \mathcal{G}(\xi))}{\Gamma(\theta)} \, d\xi, \tag{2.3} $$

where $\nu = \theta + \kappa(1 - \theta)$.

From (2.3), we define an operator $\mathbb{T} : \mathcal{X} \to \mathcal{X}$:

$$ \mathbb{T}(\mathcal{G}(t)) = \frac{\mathcal{G}_0}{\Gamma(\nu)} (\psi(t) - \psi(0))^{\nu-1} + \frac{1}{\Gamma(\theta)} \int_0^t \psi'(\xi)(\psi(t) - \psi(\xi))^{\theta-1} \Pi(\xi, \mathcal{G}(\xi)) \, d\xi. \tag{2.4} $$

Consider the following assumptions for the remaining analysis:

(A_1) There exists a constant $L_\Pi > 0$ such that for all $t \in J$ and $\mathcal{G}_1,\ \mathcal{G}_2 \in \mathcal{X}$,

$$ \|\Pi(\mathcal{G}_1) - \Pi(\mathcal{G}_2)\| \leq L_\Pi \|\mathcal{G}_1 - \mathcal{G}_2\|. $$

(A_2) There exist constants $M_\Pi,\ N_\Pi > 0$ such that for all $t \in J$ and $\mathcal{G} \in \mathcal{X}$,

$$ \|\Pi(\mathcal{G})\| \leq M_\Pi \|\mathcal{G}\| + N_\Pi. $$

2.2. Existence and uniqueness results

Theorem 2.4. *Given* (A_1) *and assuming that* $\Gamma(\theta+1) > L_\Pi(\psi(T)-\psi(0))$ *holds, then problem* (2.4) *has a unique solution on* J.

Proof. Let $\mathcal{G}_1, \mathcal{G}_2 \in \mathcal{X}$. We can write:

$$\begin{aligned}
\|\mathbb{T}\mathcal{G}_1 - \mathbb{T}\mathcal{G}_2\| &= \max_{t\in J}\Big\{\Big|\int_0^t \frac{\psi'(\xi)(\psi(t)-\psi(\xi))^{\theta-1}\Pi(\xi,\mathcal{G}_1(\xi))}{\Gamma(\theta)}\,d\xi \\
&\quad - \int_0^t \frac{\psi'(\xi)(\psi(t)-\psi(\xi))^{\theta-1}\Pi(\xi,\mathcal{G}_2(\xi))}{\Gamma(\theta)}\,d\xi\Big|\Big\} \\
&\le \max_{t\in J}\Big\{\frac{1}{\Gamma(\theta)}\Big\{\int_0^t \psi'(\xi)(\psi(t)-\psi(\xi))^{\theta-1} \\
&\quad \times|\Pi(\xi,\mathcal{G}_1(\xi)) - \Pi(\xi,\mathcal{G}_2(\xi))|\,d\xi\Big\}\Big\} \\
&\le \max_{t\in J}\Big\{\frac{L_\Pi(\psi(t)-\psi(0))^\theta}{\Gamma(\theta+1)}|\mathcal{G}_1(t)-\mathcal{G}_2(t)|\Big\} \\
&\le \frac{L_\Pi(\psi(T)-\psi(0))^\theta}{\Gamma(\theta+1)}\|\mathcal{G}_1-\mathcal{G}_2\|.
\end{aligned}$$

Since $\frac{L_\Pi(\psi(T)-\psi(0))^\theta}{\Gamma(\theta+1)} < 1$ by hypothesis, $\mathbb{T}$ is a contraction mapping on the Banach space $\mathcal{X}$. By the Banach fixed point theorem, $\mathbb{T}$ has a unique fixed point, which corresponds to the unique solution of (2.2). □

Theorem 2.5. *There is at least one solution to problem* (2.4) *for any* $T > 0$ *if assumptions* (A_1, A_2) *are true.*

Proof. We verify that $\mathbb{T}$ satisfies the conditions of Schauder's fixed point theorem.

Step 1: Continuity of $\mathbb{T}$**.** Let $\{\mathcal{G}_n\}$ be a sequence in $\mathcal{X}$ converging to $\mathcal{G}$. Then

$$\begin{aligned}
\|\mathbb{T}\mathcal{G}_n - \mathbb{T}\mathcal{G}\| &= \max_{t\in J}\Big\{\Big|\int_0^t \frac{\psi'(\xi)(\psi(t)-\psi(\xi))^{\theta-1}\Pi(\xi,\mathcal{G}_n(\xi))}{\Gamma(\theta)}\,d\xi \\
&\quad - \int_0^t \frac{\psi'(\xi)(\psi(t)-\psi(\xi))^{\theta-1}\Pi(\xi,\mathcal{G}(\xi))}{\Gamma(\theta)}\,d\xi\Big|\Big\} \\
&\le \max_{t\in J}\Big\{\frac{1}{\Gamma(\theta)}\Big\{\int_0^t \psi'(\xi)(\psi(t)-\psi(\xi))^{\theta-1} \\
&\quad \times|\Pi(\xi,\mathcal{G}_n(\xi)) - \Pi(\xi,\mathcal{G}(\xi))|\,d\xi\Big\}\Big\} \\
&\le \max_{t\in J}\Big\{\frac{L_\Pi(\psi(t)-\psi(0))^\theta}{\Gamma(\theta+1)}|\mathcal{G}_n(t)-\mathcal{G}(t)|\Big\} \\
&\le \frac{L_\Pi(\psi(T)-\psi(0))^\theta}{\Gamma(\theta+1)}\|\mathcal{G}_n-\mathcal{G}\|.
\end{aligned}$$

Hence $\|\mathbb{T}\mathcal{G}_n - \mathbb{T}\mathcal{G}\| \to 0$ as $n \to \infty$. Thus $\mathbb{T}$ is continuous.

Step 2: Boundedness. Consider $\mathcal{R} > 0$ such that

$$\left\{\frac{(\psi(T)-\psi(0))\mathcal{G}_0}{(\psi(b)-\psi(0))\Gamma(\nu)}+\frac{(M_\Pi\mathcal{R}+N_\Pi)}{\Gamma(\theta+1)}\right\}\leq\mathcal{R}$$

and define the convex subset $\mathcal{E}=\{\mathcal{G}\in\mathcal{X}:\|\mathcal{G}\|\leq\mathcal{R}\}$.

For any $\mathcal{G}\in\mathcal{E}$, we can write

$$\begin{aligned}
\|\mathbb{T}\mathcal{G}\| &= \max_{t\in J}\left|\frac{\mathcal{G}_0}{\Gamma(\nu)}(\psi(t)-\psi(0))^{\nu-1}+\frac{1}{\Gamma(\theta)}\int_0^t\psi'(\xi)(\psi(t)-\psi(\xi))^{\theta-1}\Pi(\xi,\mathcal{G}(\xi))\,d\xi\right|\\
&\leq \max_{t\in J}\left\{\left|\frac{\mathcal{G}_0}{\Gamma(\nu)}(\psi(t)-\psi(0))^{\nu-1}\right|+\frac{1}{\Gamma(\theta)}\int_0^t\psi'(\xi)(\psi(t)-\psi(\xi))^{\theta-1}|\Pi(\xi,\mathcal{G}(\xi))|\right\}d\xi\\
&\leq \left\{\frac{(\psi(T)-\psi(0))\mathcal{G}_0}{(\psi(b)-\psi(0))\Gamma(\nu)}+\frac{(M_\Pi\|\mathcal{G}\|+N_\Pi)}{\Gamma(\theta+1)}\right\}\\
&\leq \left\{\frac{(\psi(T)-\psi(0))\mathcal{G}_0}{(\psi(b)-\psi(0))\Gamma(\nu)}+\frac{(M_\Pi\mathcal{R}+N_\Pi)}{\Gamma(\theta+1)}\right\}\leq\mathcal{R}.
\end{aligned}$$

Therefore $\mathbb{T}(\mathcal{E})$ is uniformly bounded.

Step 3: Equicontinuity. For any $\mathcal{G}\in\mathcal{E}$ and $t_1<t_2$, consider

$$\begin{aligned}
\|\mathbb{T}\mathcal{G}(t_1)-\mathbb{T}\mathcal{G}(t_2)\| &= \max_{t\in J}\left|\frac{\mathcal{G}_0}{\Gamma(\nu)}(\psi(t_1)-\psi(0))^{\nu-1}+\frac{1}{\Gamma(\theta)}\int_0^{t_1}\psi'(\xi)(\psi(t_1)-\psi(\xi))^{\theta-1}\Pi(\xi,\mathcal{G}(\xi))\,d\xi\right.\\
&\quad\left.-\frac{\mathcal{G}_0}{\Gamma(\nu)}(\psi(t_2)-\psi(0))^{\nu-1}-\frac{1}{\Gamma(\theta)}\int_0^{t_2}\psi'(\xi)(\psi(t_2)-\psi(\xi))^{\theta-1}\Pi(\xi,\mathcal{G}(\xi))\,d\xi\right|.
\end{aligned}$$

As $t_1\to t_2$, we have $\|\mathbb{T}\mathcal{G}(t_1)-\mathbb{T}\mathcal{G}(t_2)\|\to 0$. Thus $\mathbb{T}$ is equicontinuous and satisfies all conditions of Schauder's fixed point theorem. Hence problem (2.4) has at least one solution. □

3. UH stability analysis

Stability analysis is crucial for understanding how perturbations affect system behavior. UH stability provides a quantitative measure of robustness. If an approximate solution is close to satisfying the equation, it must be close to some exact solution [30].

Definition 3.1. *The considered Model* (1.2) *is UH stable if there exists* $\varepsilon>0$ *such that for any* $\lambda>0$*, and any approximate solution* $\mathcal{G}^*(t)$ *satisfying*

$$\left|{}^H\mathrm{D}_{0^+}^{\theta,\kappa;\psi}\mathcal{G}^*(t)-\Pi(t,\mathcal{G}^*(t))\right|\leq\lambda,$$

there exists a unique solution $\mathcal{G}(t)$ *of the specified model with*

$$\left\|\mathcal{G}^*-\mathcal{G}\right\|\leq\varepsilon\lambda.$$

Theorem 3.2. *Consider that assumptions* (A_1,A_2) *hold. Then the considered Model* (1.2) *is UH stable if*

$$L_\Pi(\psi(T)-\psi(0))^\theta<\Gamma(\theta+1).$$

Proof. Consider a function $\mathcal{G}^*(t)$ and for $\lambda > 0$, we have

$$\left|{}^{H}\mathrm{D}_{0^+}^{\theta,\kappa;\psi}\mathcal{G}^*(t) - \Pi(t,\mathcal{G}^*(t))\right| \leq \lambda.$$

Let $P(t) \in C[0,T]$ such that for $\lambda > 0$ and $|P(t)| \leq \lambda$.

$${}^{H}\mathrm{D}_{0^+}^{\theta,\kappa;\psi}\mathcal{G}^*(t) = \Pi(t,\mathcal{G}^*(t)) + P(t). \tag{3.1}$$

The solution of Eq (3.1) becomes

$$\begin{aligned}\mathcal{G}^*(t) = {} & \frac{\mathcal{G}_0}{\Gamma(\nu)}(\psi(t)-\psi(0))^{\nu-1} + \frac{1}{\Gamma(\theta)}\int_0^t \psi'(\xi)(\psi(t)-\psi(\xi))^{\theta-1}\Pi(\xi,\mathcal{G}^*(\xi))\,d\xi \\ & + \frac{1}{\Gamma(\theta)}\int_0^t \psi'(\xi)(\psi(t)-\psi(\xi))^{\theta-1}P(\xi)\,d\xi.\end{aligned}$$

Let $\mathcal{G}(t)$ be the unique solution of our specified model:

$$\mathcal{G}(t) = \frac{\mathcal{G}_0}{\Gamma(\nu)}(\psi(t)-\psi(0))^{\nu-1} + \frac{1}{\Gamma(\theta)}\int_0^t \psi'(\xi)(\psi(t)-\psi(\xi))^{\theta-1}\Pi(\xi,\mathcal{G}(\xi))\,d\xi.$$

Now consider

$$\begin{aligned}\|\mathcal{G}^*-\mathcal{G}\| &= \max_{t\in J}\left|\frac{1}{\Gamma(\theta)}\int_0^t \psi'(\xi)(\psi(t)-\psi(\xi))^{\theta-1}\{\Pi(\xi,\mathcal{G}^*(\xi))\right. \\ &\quad \left. - \Pi(\xi,\mathcal{G}(\xi))\}d\xi + \frac{1}{\Gamma(\theta)}\int_0^t \psi'(\xi)(\psi(t)-\psi(\xi))^{\theta-1}P(\xi)\,d\xi\right| \\ &\leq \frac{L_\Pi(\psi(T)-\psi(0))^\theta}{\Gamma(\theta+1)}\|\mathcal{G}-\mathcal{G}^*\| + \frac{(\psi(T)-\psi(0))^\theta}{\Gamma(\theta+1)}\lambda.\end{aligned}$$

Solving for $\|\mathcal{G}^*-\mathcal{G}\|$:

$$\begin{aligned}\|\mathcal{G}^*-\mathcal{G}\| &\leq \frac{(\psi(T)-\psi(0))^\theta}{\Gamma(\theta+1)-L_\Pi(\psi(T)-\psi(0))^\theta}\lambda \\ \Rightarrow \|\mathcal{G}^*-\mathcal{G}\| &\leq \varepsilon\lambda,\end{aligned}$$

where

$$\varepsilon = \frac{(\psi(T)-\psi(0))^\theta}{\Gamma(\theta+1)-L_\Pi(\psi(T)-\psi(0))^\theta}.$$

Thus, our considered model is UH stable. □

4. Numerical analysis and simulations

4.1. Development of the numerical scheme

A numerical scheme is essential to our analysis due to the nonlinear nature of the problem. This numerical technique enables us to obtain approximate solutions because exact solutions are often

impossible to find for real-world problems. Through simulations, we can visualize this complex problem for better understanding and explore its different aspects.

To develop the numerical scheme [31], we consider the integral equation (2.3):

$$\mathcal{G}(t) = \frac{\mathcal{G}_0}{\Gamma(\nu)}(\psi(t) - \psi(0))^{\nu-1} + \frac{1}{\Gamma(\theta)} \int_0^t \psi'(\xi)(\psi(t) - \psi(\xi))^{\theta-1} \Pi(\xi, \mathcal{G}(\xi))\, d\xi. \tag{4.1}$$

Define the nodes as $t_j = j\Delta t,\ j = 0, 1, 2, \cdots$, where Δt is the step size. Let

$$I(t) = \int_0^t \psi'(\xi)(\psi(t) - \psi(\xi))^{\theta-1} \Pi(\xi, \mathcal{G}(\xi))\, d\xi.$$

The function $\Pi(\xi, \mathcal{G}(\xi))$ is approximated by a linear spline $S_j(\xi)$, and therefore the approximation to the integral $I(t)$ is given as:

$$\mathbb{I}(t_j) = \int_0^{t_j} S_j(\xi)(\psi(t_j) - \psi(\xi))^{\theta-1} \psi'(\xi)\, d\xi. \tag{4.2}$$

The spline $S_j(\xi)$ is given as:

$$S_j(\xi) = \sum_{\ell=0}^{j} \Pi(t_\ell, \mathcal{G}(t_\ell)) S_{j,\ell}(\xi), \tag{4.3}$$

where

$$S_{j,\ell}(\xi) = \begin{cases} \frac{\xi - t_\ell}{t_{\ell+1} - t_\ell}, & t_\ell \le \xi \le t_{\ell+1}, \\ \frac{t_{\ell+2} - \xi}{t_{\ell+2} - t_{\ell+1}}, & t_{\ell+1} \le \xi \le t_{\ell+2}, \\ 0, & \text{otherwise.} \end{cases}$$

With the help of (4.2) and (4.3), we can write

$$\mathbb{I}(t_j) = \sum_{\ell=0}^{j} \Pi(t_\ell, \mathcal{G}(t_\ell)) \int_{t_\ell}^{t_{\ell+2}} S_{j,\ell}(\xi)(\psi(t_j) - \psi(\xi))^{\theta-1} \psi'(\xi)\, d\xi. \tag{4.4}$$

After simplification, the integral equation (4.1) becomes:

$$\begin{aligned} \mathcal{G}(t_j) &= \frac{\mathcal{G}_0}{\Gamma(\nu)}(\psi(t_j) - \psi(0))^{\nu-1} + \frac{1}{\Delta t \Gamma(\theta+1)} \sum_{\ell=0}^{j} \Pi(t_\ell, \mathcal{G}(t_\ell)) \times \Big\{ (t_\ell - t_{\ell+1})(\psi(t_j) - \psi(t_\ell))^\theta \\ &\quad + (t_{\ell+2} - t_{\ell+1})(\psi(t_j) - \psi(t_\ell))^\theta + \int_{t_\ell}^{t_{\ell+2}} (\psi(t_j) - \psi(\xi))^\theta\, d\xi \Big\}. \end{aligned} \tag{4.5}$$

If we set $\psi(t) = t$, then (4.5) implies:

$$\begin{aligned} \mathcal{G}(t_j) &= \frac{\mathcal{G}_0 (t_j)^{\nu-1}}{\Gamma(\nu)} + \frac{1}{\Delta t \Gamma(\theta+1)} \sum_{\ell=0}^{j} \Pi(t_\ell, \mathcal{G}(t_\ell)) \Big\{ (t_j - t_\ell)^\theta (t_\ell - 2t_{\ell+1} + t_{\ell+2}) \\ &\quad + \frac{1}{(\theta+1)} \big((t_j - t_\ell)^{\theta+1} - (t_j - t_{\ell+2})^{\theta+1} \big) \Big\}. \end{aligned} \tag{4.6}$$

Hence, in light of (4.6), the required numerical scheme for our problem is given as:

$$\begin{cases} \mathrm{x}(t_j) &= \dfrac{\mathrm{x}_0(t_j)^{\nu-1}}{\Gamma(\nu)} + \dfrac{1}{\Delta t\,\Gamma(\theta+1)} \displaystyle\sum_{\ell=0}^{j} \Big\{\sigma(\mathrm{y}(t_\ell) - \mathrm{x}(t_\ell))\Big\} \\ &\quad \times \Big\{(t_j - t_\ell)^{\theta}(t_\ell - 2t_{\ell+1} + t_{\ell+2}) + \tfrac{1}{(\theta+1)}\Big((t_j - t_\ell)^{\theta+1} - (t_j - t_{\ell+2})^{\theta+1}\Big)\Big\}, \\ \mathrm{y}(t_j) &= \dfrac{\mathrm{y}_0(t_j)^{\nu-1}}{\Gamma(\nu)} + \dfrac{1}{\Delta t\,\Gamma(\theta+1)} \displaystyle\sum_{\ell=0}^{j} \Big\{\mathrm{x}(t_\ell)(\rho - \mathrm{z}(t_\ell)) - \mathrm{y}(t_\ell)\Big\} \\ &\quad \times \Big\{(t_j - t_\ell)^{\theta}(t_\ell - 2t_{\ell+1} + t_{\ell+2}) + \tfrac{1}{(\theta+1)}\Big((t_j - t_\ell)^{\theta+1} - (t_j - t_{\ell+2})^{\theta+1}\Big)\Big\}, \\ \mathrm{z}(t_j) &= \dfrac{\mathrm{z}_0(t_j)^{\nu-1}}{\Gamma(\nu)} + \dfrac{1}{\Delta t\,\Gamma(\theta+1)} \displaystyle\sum_{\ell=0}^{j} \Big\{\mathrm{x}(t_\ell)\mathrm{y}(t_\ell) - \beta\mathrm{z}(t_\ell)\Big\} \\ &\quad \times \Big\{(t_j - t_\ell)^{\theta}(t_\ell - 2t_{\ell+1} + t_{\ell+2}) + \tfrac{1}{(\theta+1)}\Big((t_j - t_\ell)^{\theta+1} - (t_j - t_{\ell+2})^{\theta+1}\Big)\Big\}. \end{cases} \tag{4.7}$$

4.2. Pseudocode for the numerical scheme

Algorithm 1 Numerical scheme for the ψ-Hilfer fractional Lorenz system.

procedure SolveLorenz($\sigma, \rho, \beta, \theta, \kappa, T, \Delta t, \mathrm{x}_0, \mathrm{y}_0, \mathrm{z}_0$)
  $N \leftarrow T/\Delta t$
  $\nu \leftarrow \theta + \kappa(1-\theta)$
  $t_0 \leftarrow 0$, $I_{0^+}^{(1-\theta)(1-\kappa);\psi}\mathrm{x}(0^+) \leftarrow \mathrm{x}_0$, $I_{0^+}^{(1-\theta)(1-\kappa);\psi}\mathrm{y}(0^+) \leftarrow \mathrm{y}_0$, $I_{0^+}^{(1-\theta)(1-\kappa);\psi}\mathrm{z}(0^+) \leftarrow \mathrm{z}_0$
  for $j = 0$ to $N-1$ **do**
    $t_{j+1} \leftarrow (j+1)\Delta t$
    Initialize sums for x, y, z
    for $\ell = 0$ to j **do**
      Compute coefficient $C \leftarrow (t_j - t_\ell)^{\theta}(t_\ell - 2t_{\ell+1} + t_{\ell+2})$
      Compute $D \leftarrow \frac{1}{\theta+1}((t_j - t_\ell)^{\theta+1} - (t_j - t_{\ell+2})^{\theta+1})$
      $W \leftarrow C + D$
      Update sum_x $\leftarrow$ sum_x $+\sigma(\mathrm{y}(\ell) - \mathrm{x}(\ell)) \times W$
      Update sum_y $\leftarrow$ sum_y $+(\mathrm{x}(\ell)(\rho - \mathrm{z}(\ell)) - \mathrm{y}(\ell)) \times W$
      Update sum_z $\leftarrow$ sum_z $+(\mathrm{x}(\ell)\mathrm{y}(\ell) - \beta\mathrm{z}(\ell)) \times W$
    end for
    $\mathrm{x}(j+1) \leftarrow \frac{\mathrm{x}_0 t_j^{\nu-1}}{\Gamma(\nu)} + \frac{1}{\Delta t\Gamma(\theta+1)} \times$ sum_x
    $\mathrm{y}(j+1) \leftarrow \frac{\mathrm{y}_0 t_j^{\nu-1}}{\Gamma(\nu)} + \frac{1}{\Delta t\Gamma(\theta+1)} \times$ sum_y
    $\mathrm{z}(j+1) \leftarrow \frac{\mathrm{z}_0 t_j^{\nu-1}}{\Gamma(\nu)} + \frac{1}{\Delta t\Gamma(\theta+1)} \times$ sum_z
  end for
  return $(t, \mathrm{x}, \mathrm{y}, \mathrm{z})$
end procedure

4.3. Error and convergence analysis

Let $\mathcal{G}(t_j)$ be the exact solution of (4.1) and $\mathcal{G}_j$ the numerical solution obtained from (4.7) at $t_j = j\Delta t$, where $j = 0, 1, \ldots, N$ and $\Delta t = T/N$. Define the global error $e_j = \mathcal{G}(t_j) - \mathcal{G}_j$.

Lemma 4.1. *Assume $\Pi \in C^2[0, T]$ with $\|\Pi''\| \le M_2$. Then the local truncation error $\tau_j = \mathcal{G}(t_j) - \tilde{\mathcal{G}}_j$ satisfies*

$$\|\tau_j\| \le C_\tau(\Delta t)^2, \quad \text{where} \quad C_\tau = \frac{M_2 T^\theta}{2\Gamma(\theta+1)}.$$

Proof. From (4.1) and (4.7), the error arises from approximating Π by the linear spline S_j. For $\xi \in [t_\ell, t_{\ell+1}]$, the interpolation error bound gives

$$\|\Pi(\xi, \mathcal{G}(\xi)) - S_j(\xi)\| \le \frac{M_2}{2}(\Delta t)^2.$$

Thus,

$$\begin{aligned}
\|\tau_j\| &\le \frac{1}{\Gamma(\theta)} \sum_{\ell=0}^{j-1} \int_{t_\ell}^{t_{\ell+1}} (t_j - \xi)^{\theta-1} \cdot \frac{M_2}{2}(\Delta t)^2 d\xi \\
&= \frac{M_2(\Delta t)^2}{2\Gamma(\theta+1)} \sum_{\ell=0}^{j-1} \left[(t_j - t_\ell)^\theta - (t_j - t_{\ell+1})^\theta\right] \\
&= \frac{M_2(\Delta t)^2}{2\Gamma(\theta+1)} t_j^\theta \le \frac{M_2 T^\theta}{2\Gamma(\theta+1)}(\Delta t)^2.
\end{aligned}$$

□

Lemma 4.2. *Under assumption (A_1), the global error e_j satisfies*

$$\|e_j\| \le \frac{L_\Pi}{\Gamma(\theta+1)} \sum_{\ell=0}^{j-1} \|e_\ell\| \left[(t_j - t_\ell)^\theta - (t_j - t_{\ell+1})^\theta\right] + C_\tau(\Delta t)^2. \tag{4.8}$$

Proof. Subtracting the numerical scheme from the exact equation yields

$$e_j = \frac{1}{\Gamma(\theta)} \sum_{\ell=0}^{j-1} \int_{t_\ell}^{t_{\ell+1}} (t_j - \xi)^{\theta-1} \Big[\Pi(\xi, \mathcal{G}(\xi)) - \Pi(\xi, \mathcal{G}_\ell) + \Pi(\xi, \mathcal{G}_\ell) - S_j(\xi)\Big] d\xi.$$

The second term is τ_j. For the first term, using (A_1) and the fact that

$$\int_{t_\ell}^{t_{\ell+1}} (t_j - \xi)^{\theta-1} d\xi = \frac{1}{\theta}[(t_j - t_\ell)^\theta - (t_j - t_{\ell+1})^\theta],$$

we obtain (4.8). □

Theorem 4.3. *Under assumptions (A_1), (A_2), and the smoothness condition $\Pi \in C^2[0, T]$, provided*

$$\frac{L_\Pi T^\theta}{\Gamma(\theta+1)} < 1,$$

the numerical scheme (4.7) *converges with order* $O((\Delta t)^2)$. *Specifically,*

$$\max_{0\le j\le N} \|\mathcal{G}(t_j) - \mathcal{G}_j\| \le C(\Delta t)^2,$$

where

$$C = \frac{M_2 T^\theta}{2\Gamma(\theta+1)\left(1 - \frac{L_\Pi T^\theta}{\Gamma(\theta+1)}\right)}.$$

Proof. We prove by induction that $\|e_j\| \le C(\Delta t)^2$ for all $j = 0, 1, \ldots, N$.

For $j = 0$, the initial condition is exactly given as $\mathcal{G}_0$. Thus, $\mathcal{G}(t_0) = \mathcal{G}_0$ and consequently $e_0 = 0$. Therefore, $\|e_0\| = 0 \le C(\Delta t)^2$ holds for any $C > 0$.

Consider $\|e_\ell\| \le C(\Delta t)^2$ for all $\ell = 0, 1, \ldots, j-1$. Substituting into (4.8):

$$\begin{aligned}
\|e_j\| &\le \frac{L_\Pi}{\Gamma(\theta+1)} \sum_{\ell=0}^{j-1} C(\Delta t)^2 \left[(t_j - t_\ell)^\theta - (t_j - t_{\ell+1})^\theta\right] + C_\tau(\Delta t)^2 \\
&= C(\Delta t)^2 \cdot \frac{L_\Pi}{\Gamma(\theta+1)} t_j^\theta + C_\tau(\Delta t)^2 \\
&\le C(\Delta t)^2 \cdot \frac{L_\Pi T^\theta}{\Gamma(\theta+1)} + C_\tau(\Delta t)^2.
\end{aligned}$$

Choosing $C = \dfrac{C_\tau}{1 - \frac{L_\Pi T^\theta}{\Gamma(\theta+1)}}$ yields $\|e_j\| \le C(\Delta t)^2$, completing the induction. □

4.4. Equilibrium and stability analysis

The equilibrium points of Model (1.2) are obtained by setting ${}^H\mathrm{D}_{0^+}^{\theta,\kappa;\psi}\mathrm{x}(t) = {}^H\mathrm{D}_{0^+}^{\theta,\kappa;\psi}\mathrm{y}(t) = {}^H\mathrm{D}_{0^+}^{\theta,\kappa;\psi}\mathrm{z}(t) = 0$, which yields the same equilibria as the integer-order system:

$$E_0 = (0,0,0), \quad E_\pm = \left(\pm\sqrt{\beta(\rho-1)}, \pm\sqrt{\beta(\rho-1)}, \rho-1\right). \tag{4.9}$$

For the parameters $\sigma = 10, \rho = 28, \beta = 8/3$, the nontrivial equilibria are $E_\pm \approx (\pm 8.485, \pm 8.485, 27)$.

The Jacobian matrix of the Lorenz system is:

$$J = \begin{bmatrix} -\sigma & \sigma & 0 \\ \rho - z & -1 & -x \\ y & x & -\beta \end{bmatrix}. \tag{4.10}$$

At the trivial equilibrium $E_0 = (0,0,0)$, the eigenvalues are $\lambda_1 = -\beta = -2.667$, $\lambda_{2,3} = -\frac{\sigma+1}{2} \pm \sqrt{(\sigma+1)^2/4 + \sigma(\rho-1)} \approx -22.85$ and 11.85. The positive eigenvalue $\lambda_3 \approx 11.85 > 0$ renders E_0 a saddle point (unstable) for all fractional orders θ.

At the nontrivial equilibria $E_\pm$, the characteristic equation yields one negative real eigenvalue and two complex conjugate eigenvalues with positive real parts for the integer-order case. For fractional-order systems, an equilibrium is asymptotically stable if all eigenvalues satisfy $|\arg(\lambda_i)| > \theta\pi/2$. The positive real parts of the complex eigenvalues make $E_\pm$ unstable for θ near 1, but may stabilize for sufficiently small θ. This theoretical prediction aligns with the Lyapunov exponent estimates in Table 3, where negative exponents (stable dynamics) are observed for $\theta \le 0.95$ and positive exponents (chaos) emerge at $\theta = 0.99$ for $\kappa \ge 0.5$.

4.5. *Chaos quantification and bifurcation behavior*

The Lyapunov exponent estimates in Table 3 quantify the chaotic behavior of the system. For $\theta \leq 0.95$, negative Lyapunov exponents (-960 to -149) indicate stable or periodic dynamics. At $\theta = 0.99$, the Lyapunov exponents become positive for $\kappa \geq 0.5$ (50.99 for $\kappa = 0.5$, 77.11 for $\kappa = 1.0$), confirming the transition to chaos. This demonstrates that the fractional order θ and the Hilfer parameter κ significantly influence the dynamical behavior of the system.

Although a detailed bifurcation analysis is beyond the scope of this work, the Lyapunov exponent variation with respect to θ in Table 3 suggests bifurcation points near $\theta = 0.95$–0.99, where the exponents transition from negative to positive. A comprehensive bifurcation analysis with respect to θ and κ is recommended for future investigation.

4.6. *Simulation results and discussion*

The numerical scheme (4.7) is implemented in MATLAB to simulate the dynamics of the ψ-Hilfer fractional Lorenz system. All simulations use the parameter values $\sigma = 10$, $\rho = 28$, $\beta = 8/3$, with initial conditions $(x_0, y_0, z_0) = (1, 1, 1)$ over the time interval $t \in [0, 30]$. The step size is taken as $\Delta t = 0.01$.

4.6.1. Integer-order case ($\theta = 1, \kappa = 1$)

Figures 1–4 illustrate the impact of fixed fractional order and fixed fractal dimension on the dynamic behavior of $x(t)$, $y(t)$, and $z(t)$ over time. When both parameters are integers, the model exhibits oscillations characteristic of the Lorenz chaotic attractor, with aperiodic fluctuations across all three variables. Figure 5 shows the phase portraits of $x(t)$, $y(t)$, and $z(t)$, revealing the characteristic butterfly-shaped attractor of the Lorenz system.

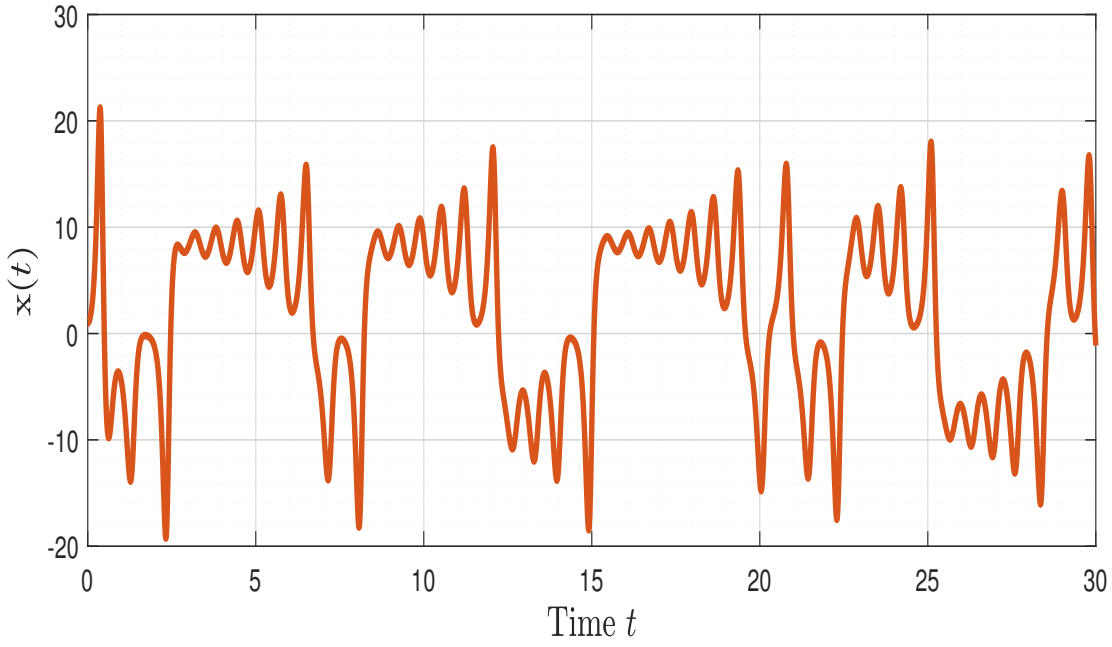

Figure 1. Evolution of x at $\theta = 1$ and $\kappa = 1$.

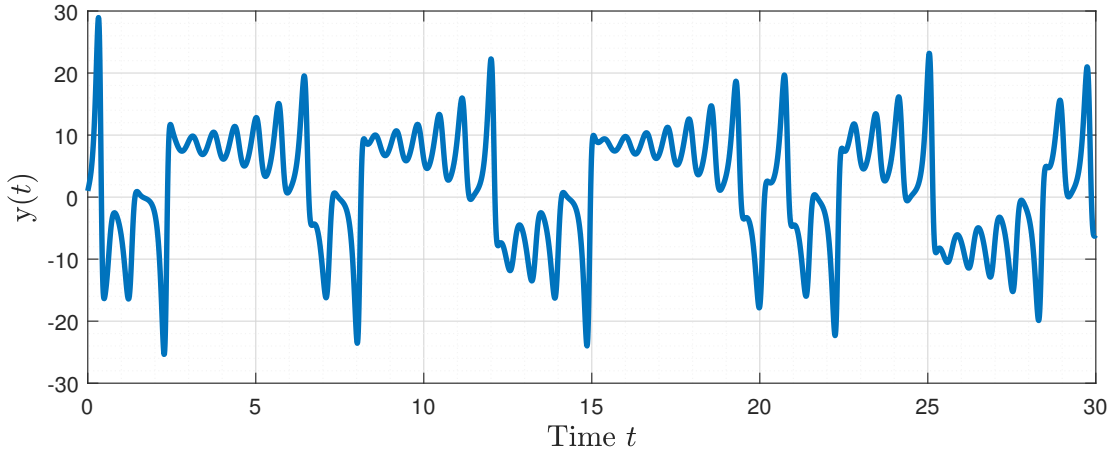

Figure 2. Evolution of y at $\theta = 1$ and $\kappa = 1$.

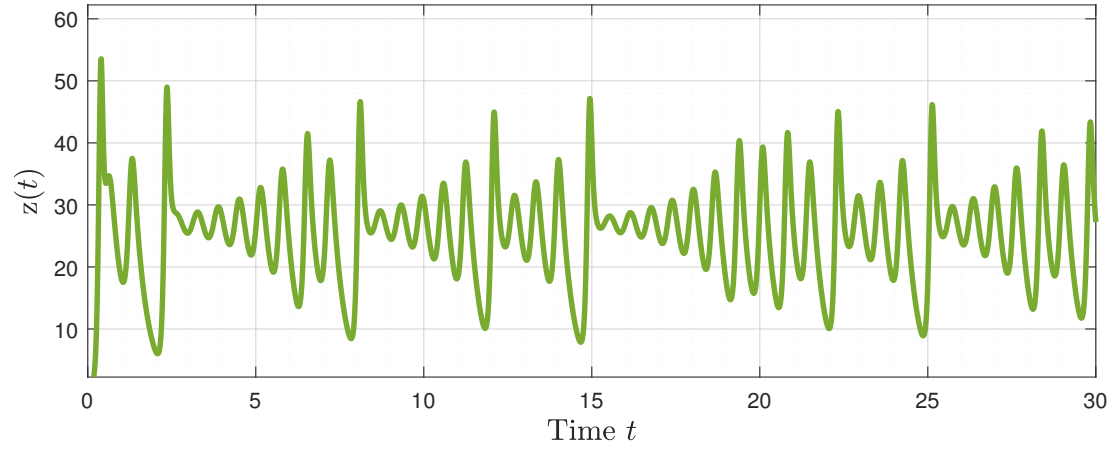

Figure 3. Evolution of z at $\theta = 1$ and $\kappa = 1$.

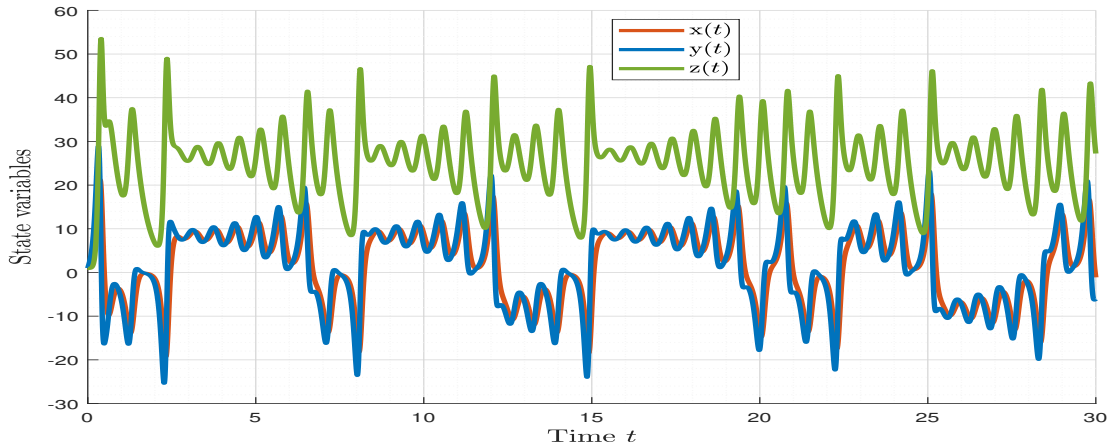

Figure 4. Combined time series evolution at $\theta = 1$ and $\kappa = 1$.

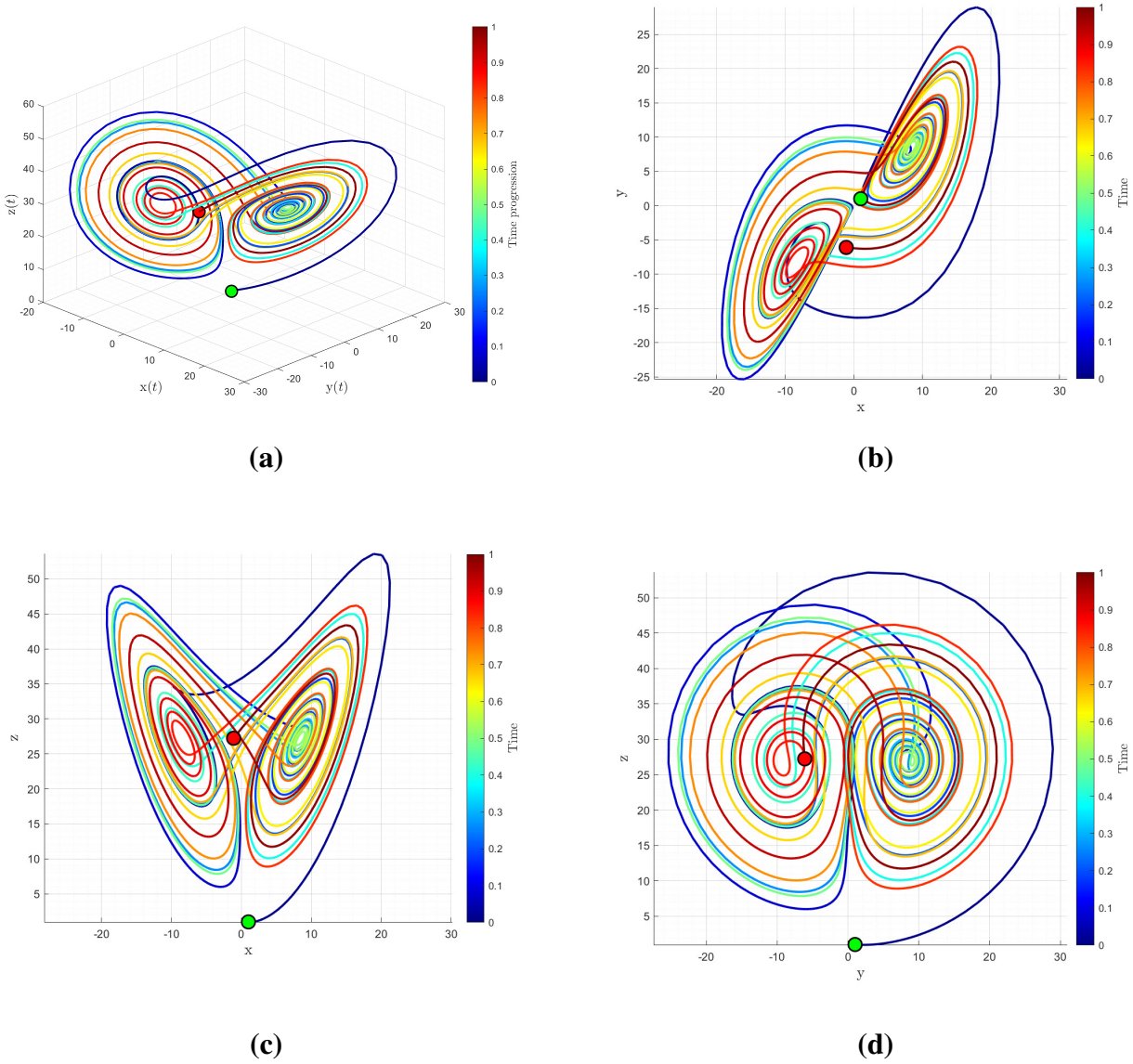

(a) **(b)**

(c) **(d)**

Figure 5. Phase portraits for $\theta = \kappa = 1$: (a) 3D attractor; (b) XY plane; (c) XZ plane; (d) YZ plane.

4.6.2. Fractional-order cases

As shown in Figures 6–10, reducing θ to 0.99 with $\kappa = 1$ yields dynamics nearly identical to the integer-order case $\theta = \kappa = 1$ in Figures 1–5. Figure 11 shows that reducing θ to 0.95 introduces a significant variation in the solution curves. Memory effects become apparent, transforming the chaotic trajectories into regular patterns with lower amplitudes. The butterfly-shaped attractor disappears by Figure 12.

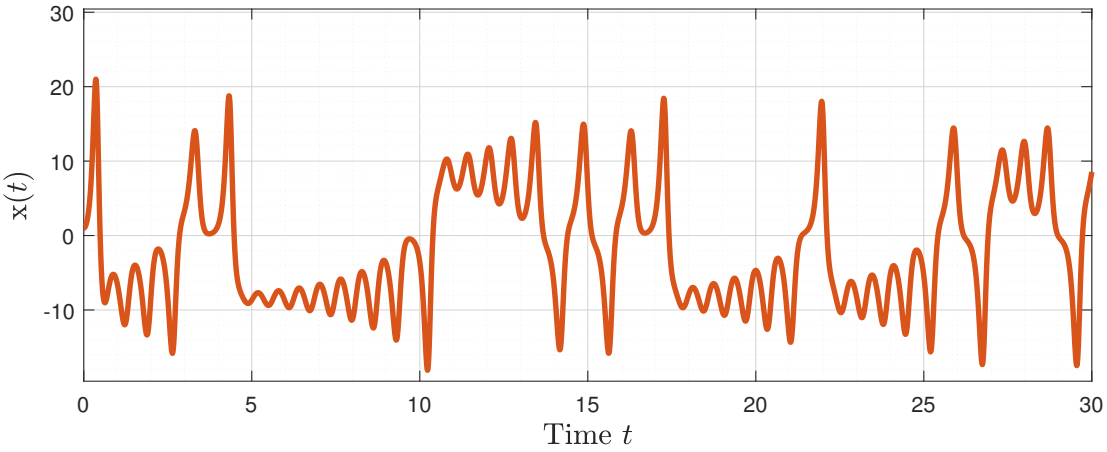

Figure 6. Evolution of x at $\theta = 0.99$ and $\kappa = 1$.

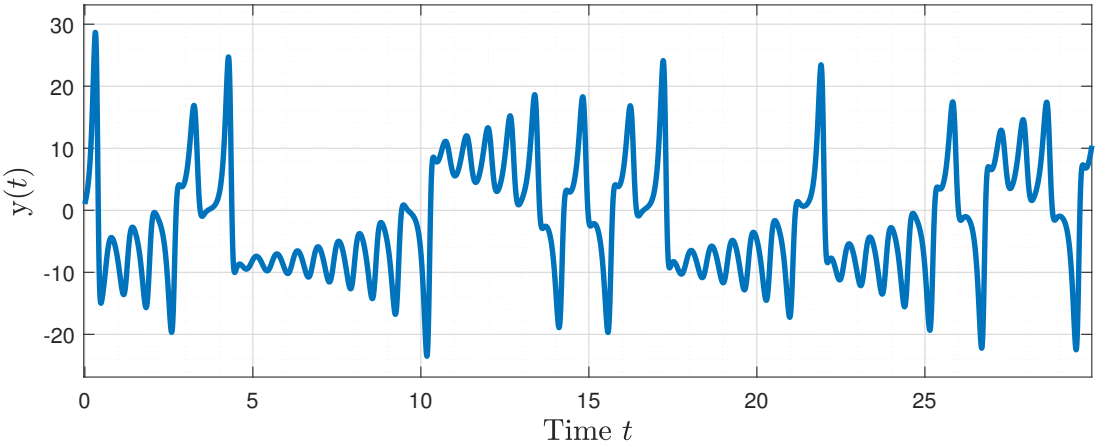

Figure 7. Evolution of y at $\theta = 0.99$ and $\kappa = 1$.

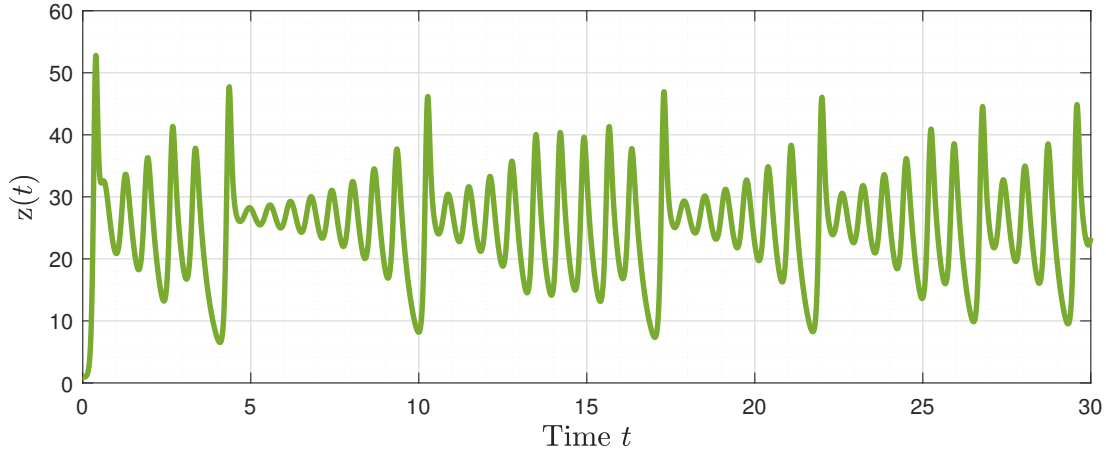

Figure 8. Evolution of z at $\theta = 0.99$ and $\kappa = 1$.

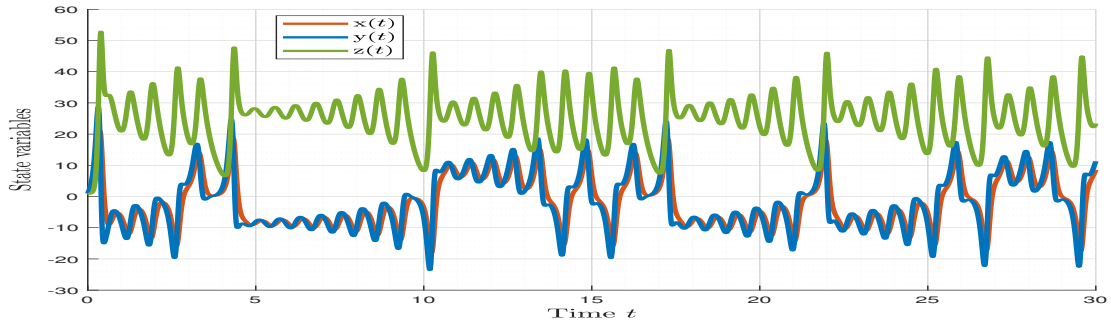

Figure 9. Combined time series evolution at $\theta = 0.99$ and $\kappa = 1$.

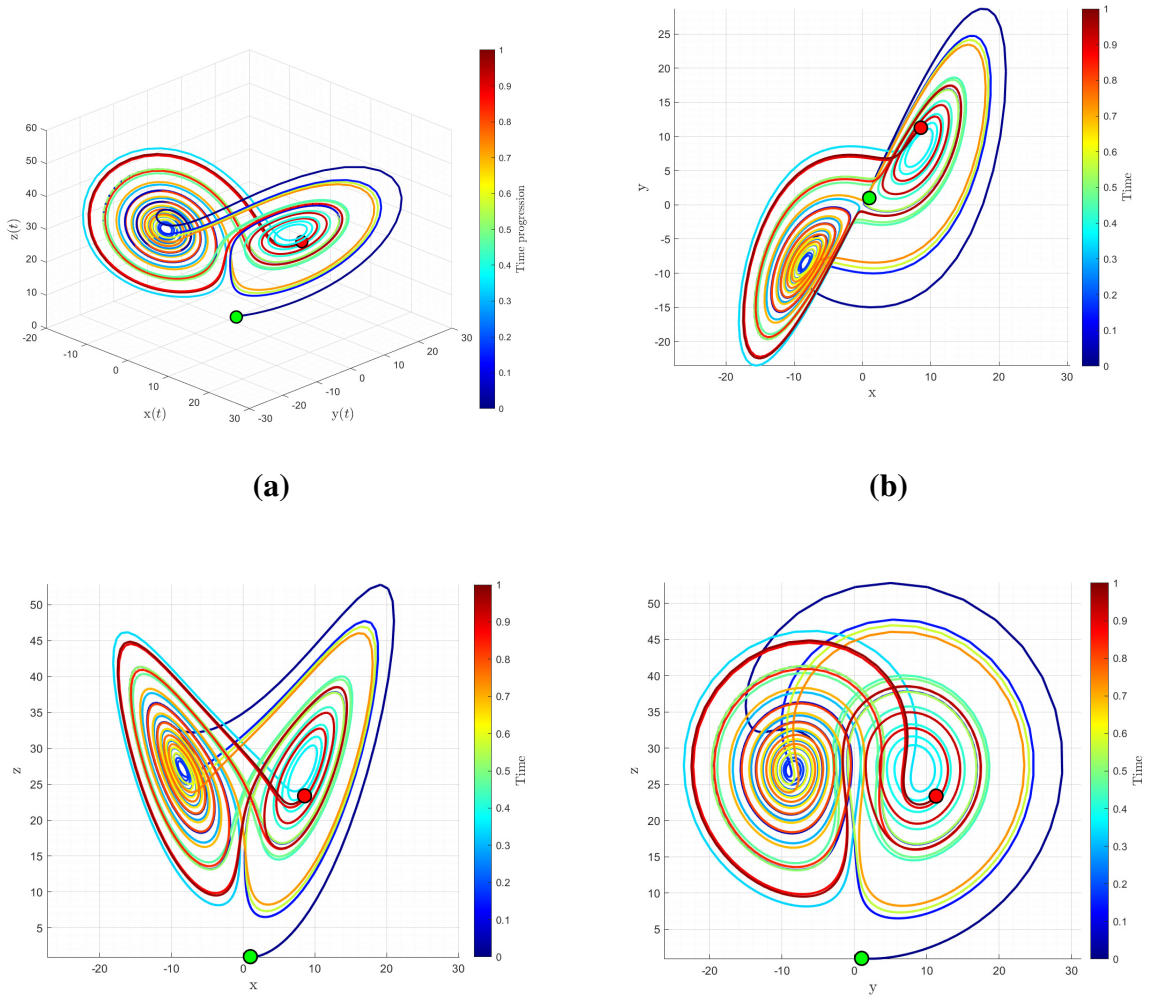

Figure 10. Phase portraits for $\theta = 0.99$, $\kappa = 1$: (a) 3D attractor; (b) XY plane; (c) XZ plane; (d) YZ plane.

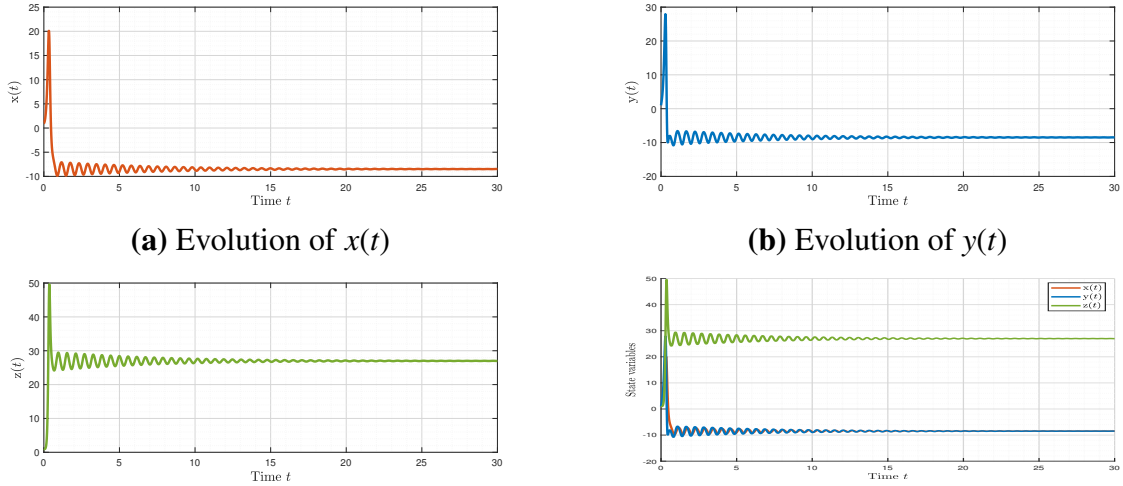

(a) Evolution of $x(t)$ **(b)** Evolution of $y(t)$

(c) Evolution of $z(t)$ **(d)** Combined evolution

Figure 11. Time series of the ψ-Hilfer fractional Lorenz system for $\theta = 0.95$ and $\kappa = 1$: (a) $x(t)$, (b) $y(t)$, (c) $z(t)$, (d) combined view.

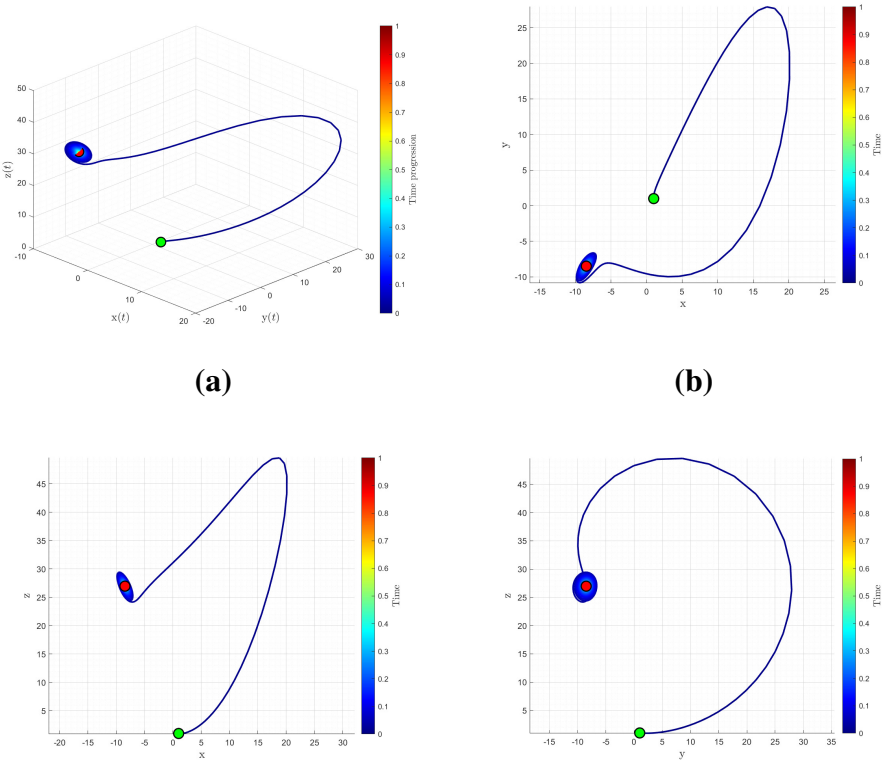

(a) **(b)**

(c) **(d)**

Figure 12. Phase portraits for $\theta = 0.95$, $\kappa = 1$: (a) 3D attractor; (b) XY plane; (c) XZ plane; (d) YZ plane.

This behavior demonstrates that decreasing the fractional order enhances the mean-reverting characteristics of the system, thereby restraining volatility. In simpler terms, this corresponds to increased persistence of past conditions and a smoothing effect over time.

It is important to note that while θ governs the fractional order and directly influences the system's memory dependence, κ affects only the scaling of initial conditions and does not alter the underlying dynamics.

5. Neural network approximation

5.1. Dataset generation

The training data for the neural network is generated using the numerical scheme developed in Section 4. For each state variable x(t), y(t), and z(t), we generate 3001 data points over the time interval $t \in [0, 30]$ with step size $\Delta t = 0.01$. The dataset is randomly partitioned into three subsets: 70% for training, 15% for validation, and 15% for testing.

5.2. Neural network architecture

We employ a feedforward neural network with the following architecture:

- Input layer: 1 neuron (time t);
- Hidden layer 1: 15 neurons with a hyperbolic tangent (tanh) activation function;
- Hidden layer 2: 15 neurons with a hyperbolic tangent (tanh) activation function;
- Output layer: 1 neuron (representing one state variable).

The mathematical expression for forward propagation is:

$$\mathbf{h}^{(1)} = \tanh(\mathbf{W}^{(1)}t + \mathbf{b}^{(1)}),$$

$$\mathbf{h}^{(2)} = \tanh(\mathbf{W}^{(2)}\mathbf{h}^{(1)} + \mathbf{b}^{(2)}),$$

$$\hat{y} = \mathbf{W}^{(3)}\mathbf{h}^{(2)} + \mathbf{b}^{(3)},$$

where $\mathbf{W}^{(i)}$ and $\mathbf{b}^{(i)}$ are weight matrices and bias vectors for layer i respectively, and tanh is the hyperbolic tangent activation function.

5.3. Training algorithm

Training employs the Levenberg-Marquardt algorithm (`trainlm`), which is a variant of gradient descent optimized for mean squared error minimization. The algorithm updates weights according to:

$$\mathbf{w}_{k+1} = \mathbf{w}_k - [\mathbf{J}^T\mathbf{J} + \mu\mathbf{I}]^{-1}\mathbf{J}^T\mathbf{e},$$

where $\mathbf{J}$ is the Jacobian matrix of errors, μ is the damping parameter, $\mathbf{I}$ is the identity matrix, and $\mathbf{e}$ is the error vector.

Training parameters are:

- Maximum epochs: 1000;
- Performance goal: 10^{-8} MSE;
- Minimum gradient: 10^{-8};

- Maximum validation failures: 20 (early stopping).

Three separate networks are trained independently to approximate each of the state variables x(t), y(t), and z(t).

5.4. *Performance metrics*

The following metrics are used to evaluate neural network performance:

- **Mean squared error (MSE)**: MSE $= \frac{1}{n}\sum_{i=1}^{n}(y_i - \hat{y}_i)^2$;
- **Root mean squared error (RMSE)**: RMSE $= \sqrt{\text{MSE}}$;
- **Mean absolute error (MAE)**: MAE $= \frac{1}{n}\sum_{i=1}^{n}|y_i - \hat{y}_i|$;
- **R-squared score**: $R^2 = 1 - \frac{\sum_{i=1}^{n}(y_i - \hat{y}_i)^2}{\sum_{i=1}^{n}(y_i - \bar{y})^2}$;
- **Maximum absolute error**: $\max_i |y_i - \hat{y}_i|$.

5.5. *Results and discussion*

Figure 13 displays the data division and best fit for the neural network output of x(t). Figures 14 and 15 show the network architecture and error analysis for x(t), respectively.

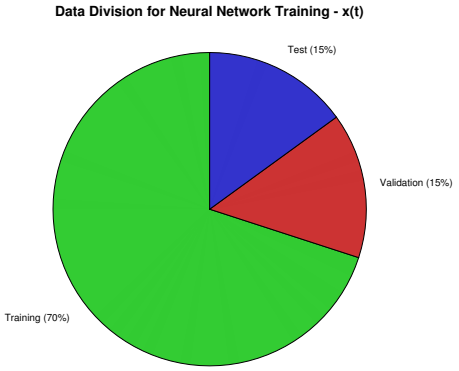

(a) Data division for neural network: x(t).

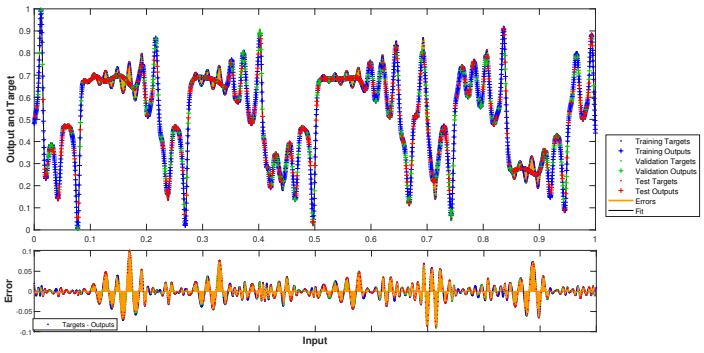

(b) Best fit for x(t) outputs.

Figure 13. Training data distribution and model fit.

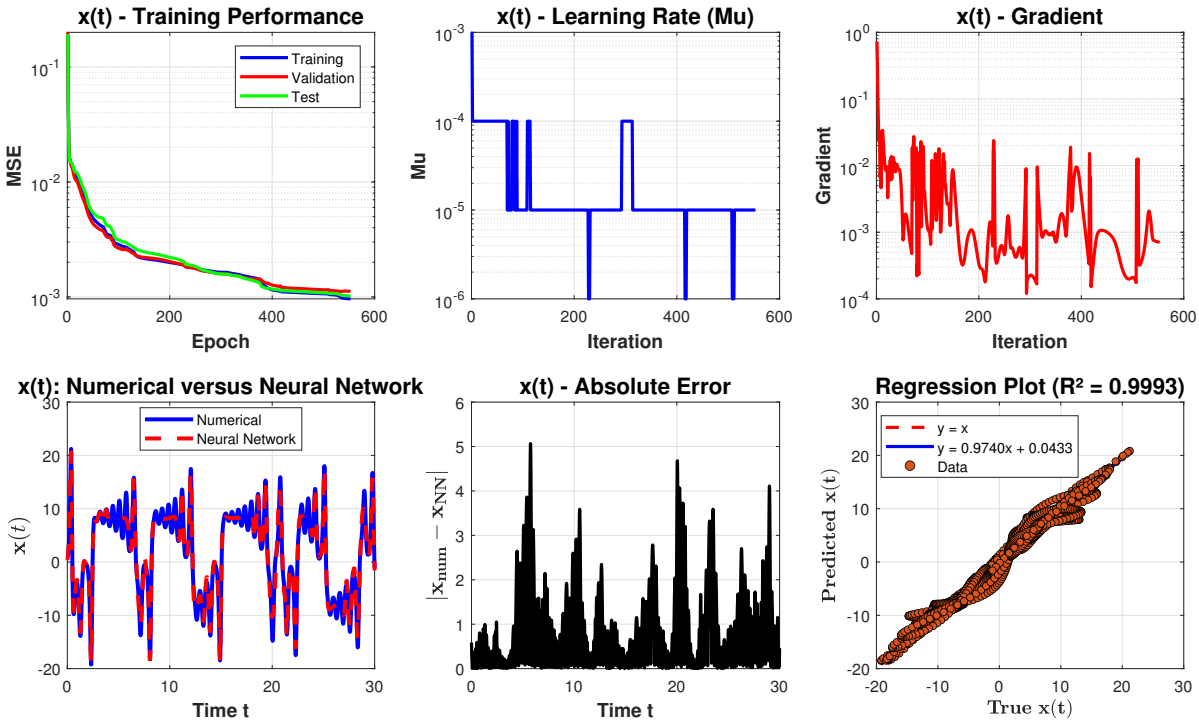

Figure 14. Neural network analysis of x(t).

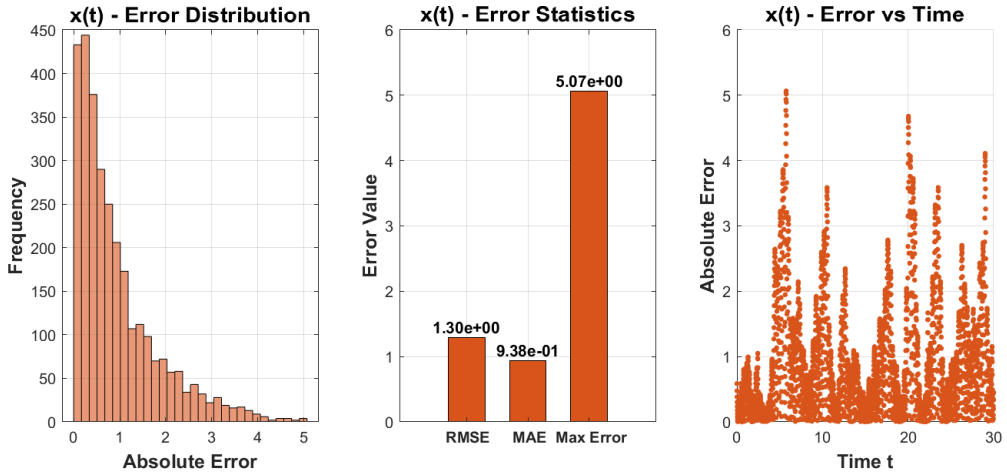

Figure 15. Error analysis of x(t).

Figure 16 illustrates the data division and best fit for the neural network output of y(t). Figures 17 and 18 present the neural network architecture and error analysis for y(t), respectively.

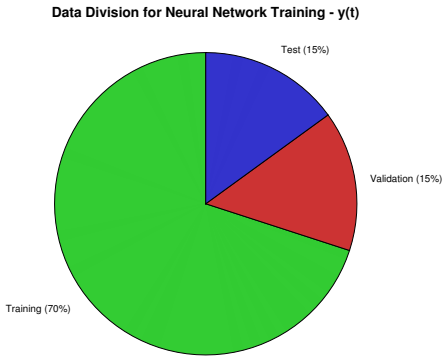

(a) Data division for neural network: y(t).

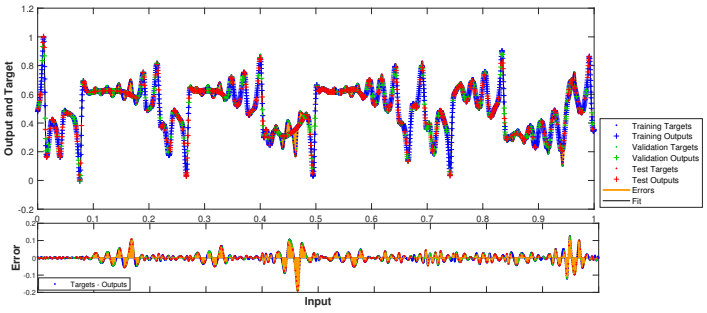

(b) Best fit for y(t) outputs.

Figure 16. Training data distribution and model fit.

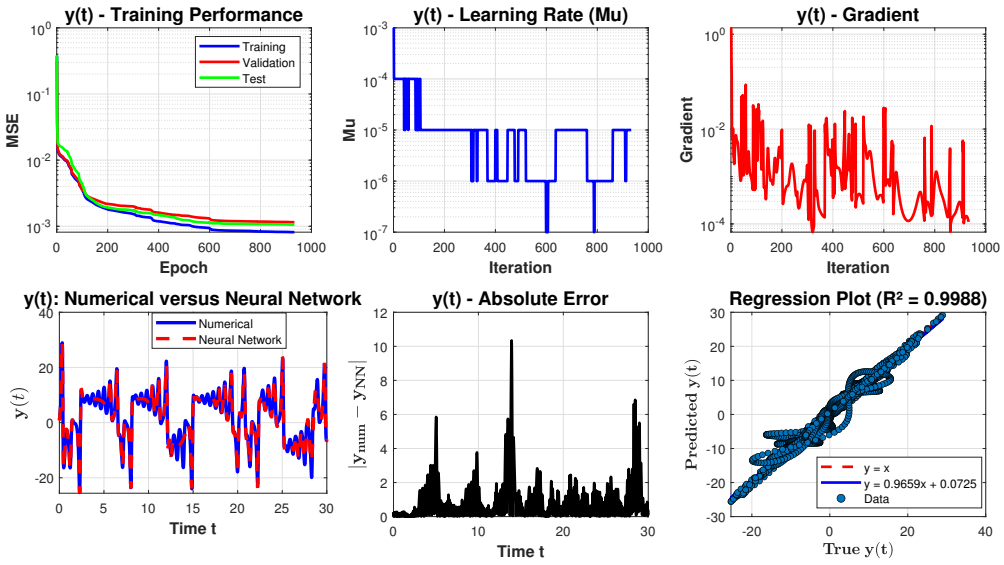

Figure 17. Neural network analysis of y(t).

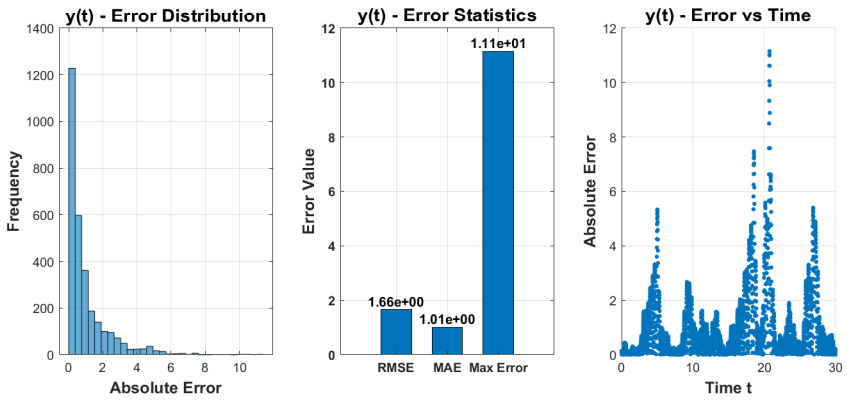

Figure 18. Error analysis of y(t).

Figure 19 illustrates the data division and best fit for the neural network output of z(t). Figures 20

and 21 present the neural network architecture and error analysis for z(t), respectively.

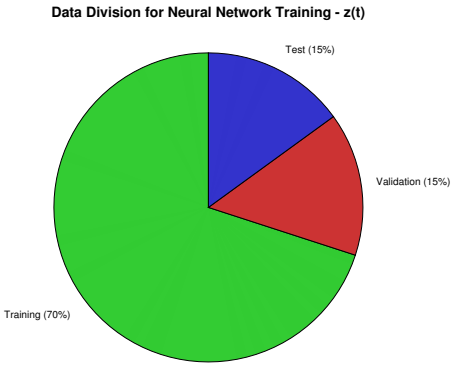

(a) Data division for neural network: z(t).

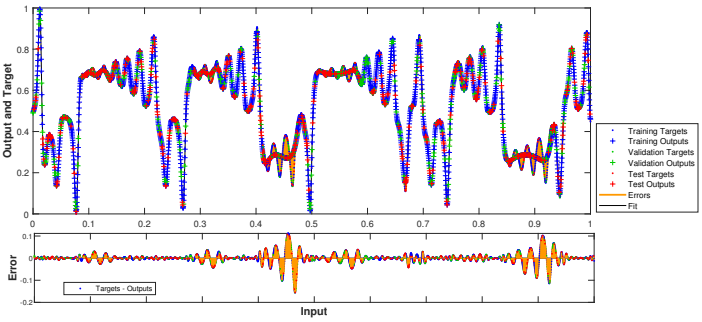

(b) Best fit for z(t) outputs.

Figure 19. Training data distribution and model fit.

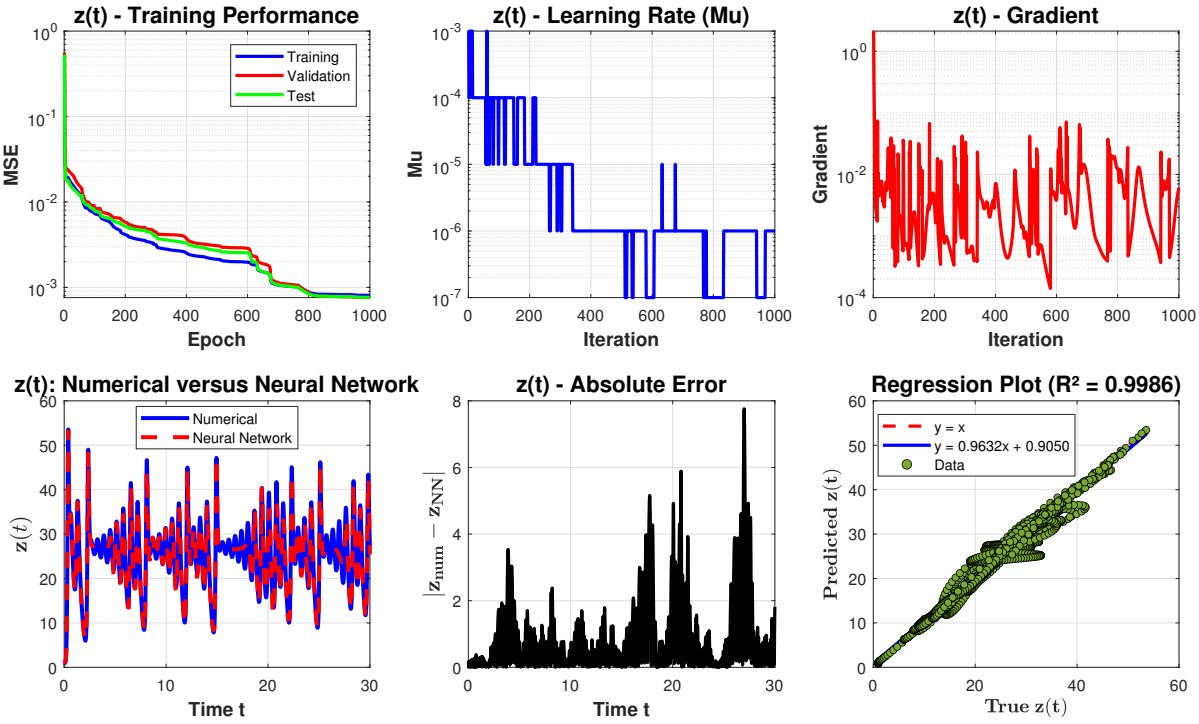

Figure 20. Neural network analysis of z(t).

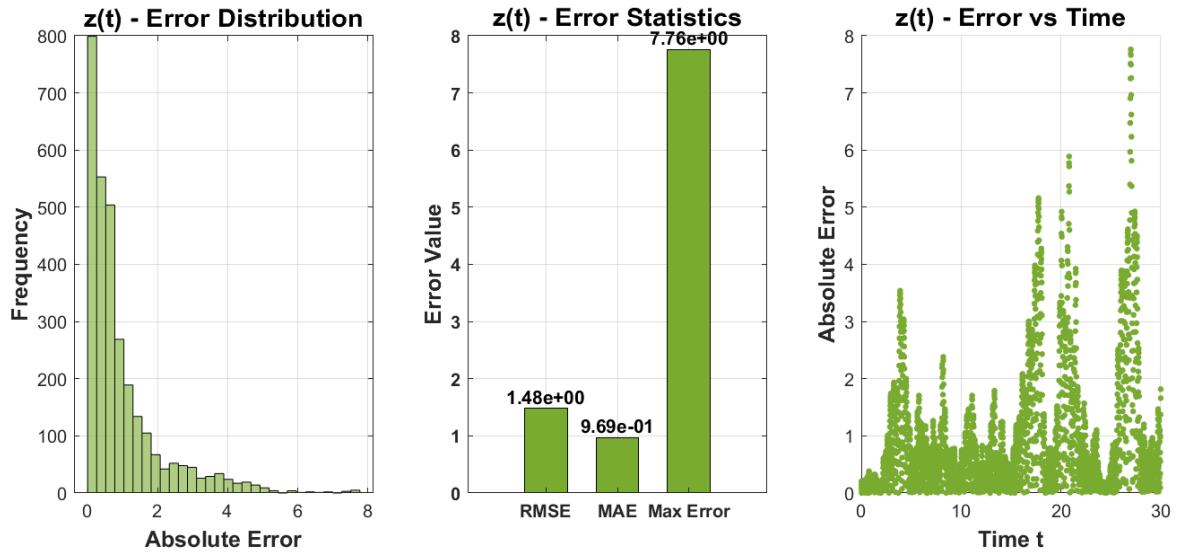

Figure 21. Error analysis of z(t).

Table 1 presents comparative performance metrics for neural network approximation of all solutions of the considered model.

Table 1. Comparative performance metrics for neural network approximation of x(t), y(t), and z(t).

Metric	x(t)	y(t)	z(t)
Performance metrics			
MSE	1.678	2.662	2.197
RMSE	1.295	1.632	1.482
MAE	0.938	1.061	0.969
R^2 Score	0.9675	0.966	0.999
Max absolute error	5.066	10.343	7.761
Regression analysis			
Regression equation	$y = 0.9740x + 0.0433$	$y = 0.9659x + 0.0725$	$y = 0.9632x + 0.9050$
Regression R^2	0.9993	0.9988	0.9986
Training statistics			
Number of epochs	552	932	1000
Final gradient	7.025×10^{-4}	1.1037×10^{-4}	6.003×10^{-3}
Final Mu	1.000×10^{-5}	1.000×10^{-5}	1.000×10^{-6}

Figure 22 presents a detailed comparison between the numerical solution and neural network prediction across all phase space projections, along with the corresponding Euclidean distance errors. It is evident from the figure that the neural network predictions are nearly identical to the numerical solutions, confirming the high accuracy of the trained model.

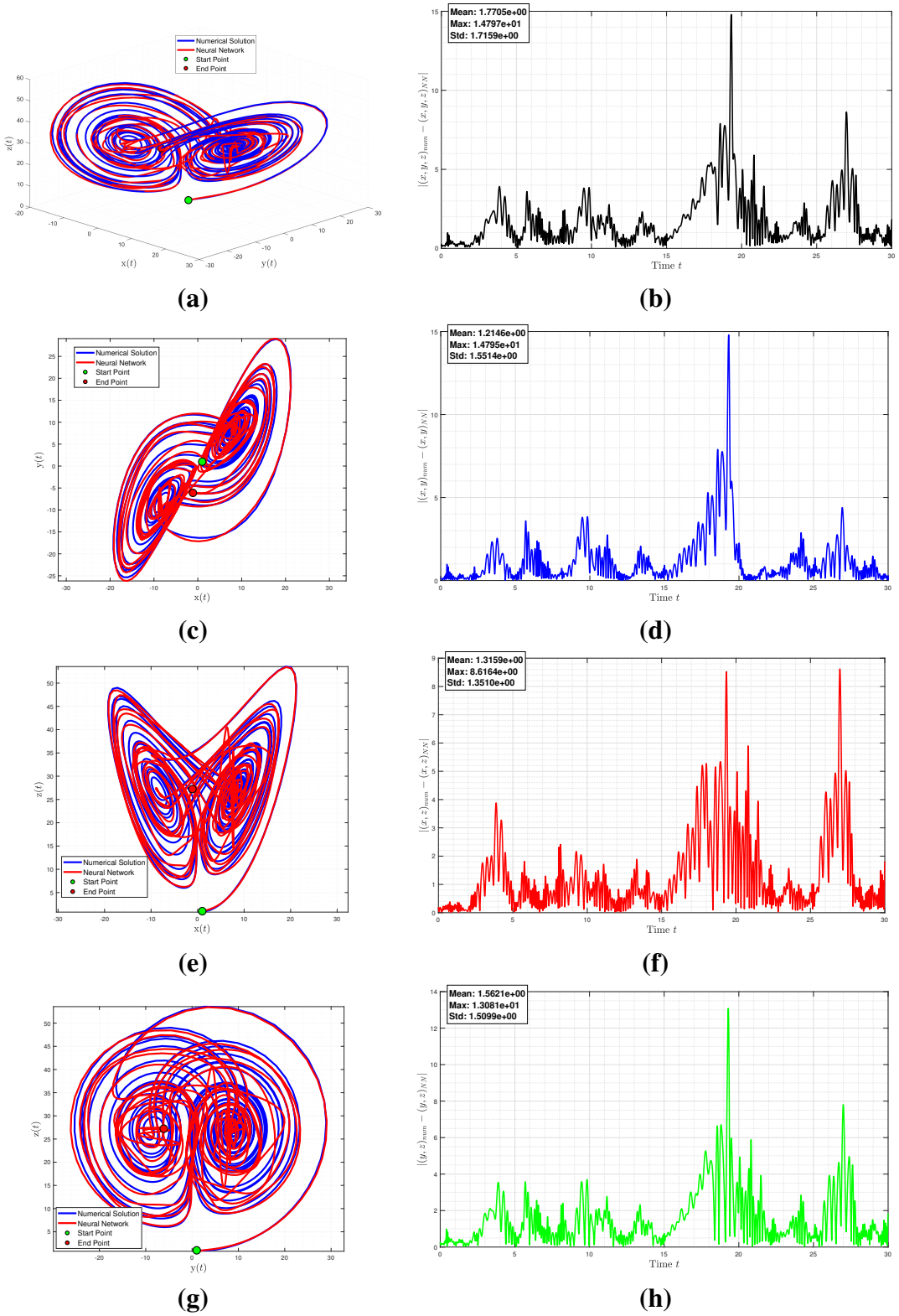

Figure 22. Phase portraits for $\theta = \kappa = 1$: (a) 3D comparison of numerical and neural network; (b) 3D Euclidean distance error; (c) XY plane comparison of numerical and neural network; (d) XY plane Euclidean distance error; (e) XZ plane comparison of numerical and neural network; (f) XZ plane Euclidean distance error; (g) YZ plane comparison of numerical and neural network; (h) YZ plane Euclidean distance error.

Table 2 provides statistics that quantify the accuracy of the neural network in approximating the solutions of the ψ-Hilfer fractional Lorenz system. The XZ plane exhibits the best performance, with the lowest maximum error (8.62), while the XY plane and 3D space yield the highest maximum errors (14.8).

Table 2. Error statistics for neural network approximation in phase space.

Error Type	Mean	Maximum	Standard Deviation
3D Space Error	1.771	14.80	1.716
XY Plane Error	1.215	14.80	1.551
XZ Plane Error	1.316	8.616	1.351
YZ Plane Error	1.562	13.08	1.510

As shown in Figures 23–25, the neural network exhibits excellent predictive capability for the considered system, with MSE values decreasing substantially from $\theta = 1.00$ to $\theta = 0.80$, achieving near-perfect approximation at the lowest fractional order.

It is clear from the close agreement between predicted and numerical trajectories that the neural network is capable of capturing the dynamics of the considered fractional Lorenz model with significant accuracy.

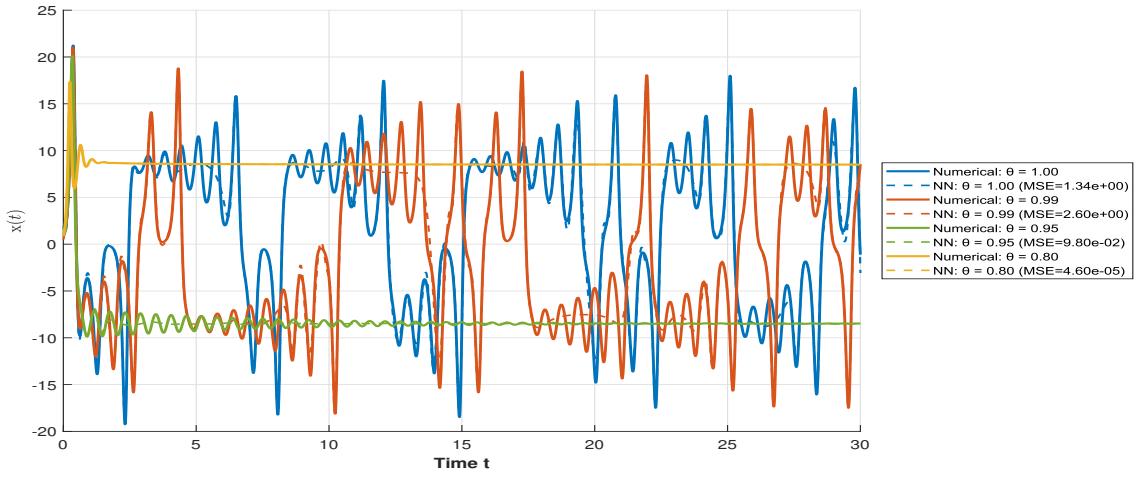

Figure 23. Comparison of numerical and neural network predictions of x(t) for $\kappa = 1$ and different values of θ.

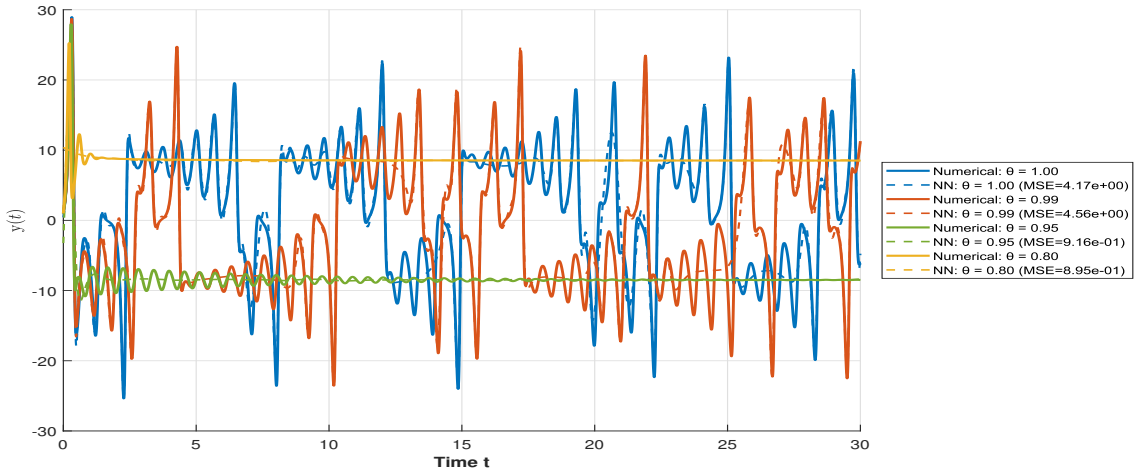

Figure 24. Comparison of numerical and neural network predictions of y(t) for $\kappa = 1$ and different values of θ.

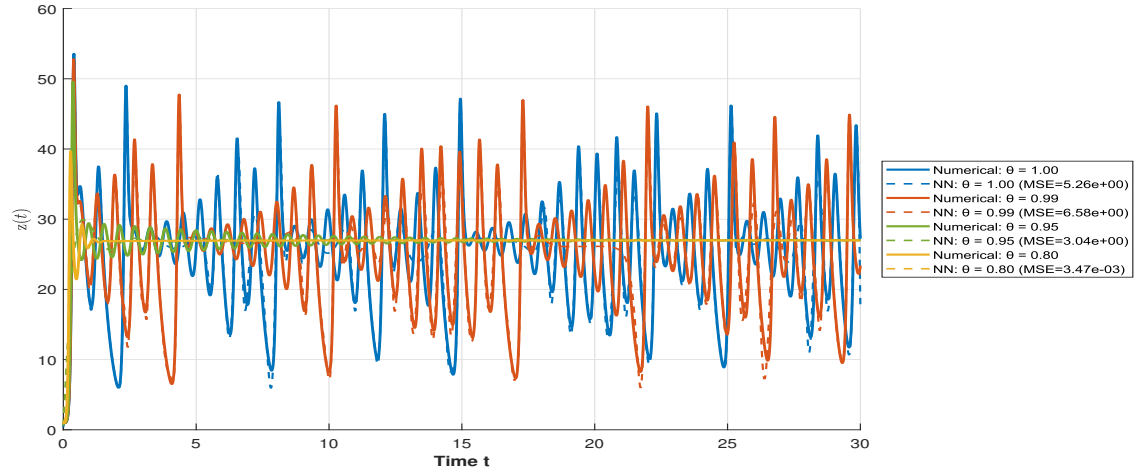

Figure 25. Comparison of numerical and neural network predictions of z(t) for $\kappa = 1$ and different values of θ.

6. Comparative analysis

6.1. Comparison with classical Lorenz systems

Classical integer-order Lorenz models focus primarily on sensitivity to initial conditions, the butterfly effect, and strange attractors. Fractional-order models, in contrast, provide more degrees of freedom and incorporate memory effects that are essential for accurately representing many real-world systems [4]. The ψ-Hilfer fractional operator provides more generalization through the two additional parameters (θ, κ), expanding the parameter space from three (σ, ρ, β) to five, enabling capture of richer dynamical behaviors absent in integer-order systems [7].

6.2. Comparison with other fractional operators

The quantitative comparison in Table 3 demonstrates three important findings. First, the ψ-Hilfer derivative with $\kappa = 0$ shows strong agreement with the classical Caputo derivative, with MSE values below 10^{-1} for $\theta \leq 0.95$ and maximum deviations on the order of 1–10. This validates both the theoretical equivalence between the two formulations when $\kappa = 0$ and the correctness of our numerical implementation. Second, the Atangana-Baleanu-Caputo (ABC) derivative exhibits systematically larger deviations from both Caputo and Hilfer methods (MSE ranging from 1 to 10^2), which is expected due to its fundamentally different exponential memory kernel compared to the power-law memory of Caputo and Hilfer. Third, the Lyapunov exponent estimates transition from large negative values (indicating stable/periodic behavior) to positive values near $\theta = 0.99$ for $\kappa = 0.5$ and 1.0, revealing that the fractional order significantly influences the chaotic dynamics of the Lorenz system, with the ψ-Hilfer operator providing tunable sensitivity through the κ parameter.

Table 3. Quantitative comparison of ψ-Hilfer, Caputo, and ABC fractional derivatives for the Lorenz system.

ψ-Hilfer Parameters		Hilfer	Hilfer versus		Hilfer versus	Hilfer
θ	κ	Time (sec)	Caputo (MSE)	ABC (MSE)	Max Dev (versus Caputo)	Lyapunov
0.700	0.0	0.6747	1.10×10^{-1}	3.07	4.54	−960.50
0.700	0.5	0.6429	3.13×10^{-2}	3.03	2.45	−887.00
0.700	1.0	0.6410	0.00	2.98	0.00	−800.88
0.800	0.0	0.6663	9.40×10^{-2}	4.76×10	3.52	−948.56
0.800	0.5	0.6626	2.51×10^{-2}	4.76×10	1.82	−885.17
0.800	1.0	0.6484	0.00	4.76×10	0.00	−808.39
0.850	0.0	0.6420	8.55×10^{-2}	5.47×10	3.23	−914.83
0.850	0.5	0.6424	2.22×10^{-2}	5.47×10	1.67	−858.15
0.850	1.0	0.6390	0.00	5.46×10	0.00	−790.15
0.900	0.0	0.6398	6.04×10^{-2}	8.98×10	2.64	−775.54
0.900	0.5	0.6414	1.57×10^{-2}	8.97×10	1.34	−727.15
0.900	1.0	0.6386	0.00	8.97×10	0.00	−671.43
0.950	0.0	0.6378	1.92×10^{-2}	8.98×10	1.62	−213.21
0.950	0.5	0.6391	4.84×10^{-3}	8.98×10	8.14×10^{-1}	−181.91
0.950	1.0	0.6391	0.00	8.97×10	0.00	−149.78
0.990	0.0	0.6397	1.36×10^2	6.22×10	3.51×10	−7.23
0.990	0.5	0.6379	7.64×10	6.86×10	3.16×10	50.99
0.990	1.0	0.6405	0.00	7.32×10	0.00	77.11

The theoretical comparison in Table 4 shows that the ψ-Hilfer operator offers maximum flexibility, encompassing Caputo ($\kappa = 0$, $\psi(t) = t$), Riemann-Liouville ($\kappa = 1$, $\psi(t) = t$), and Hadamard ($\psi(t) = \ln t$) derivatives as special cases [6, 7].

Table 4. Theoretical comparison of fractional operators: Flexibility and memory characteristics.

Operator	Parameters	Memory Kernel	Generalization
Caputo	1 (θ)	Power-law	Standard
Riemann-Liouville	1 (θ)	Power-law	Standard
Hadamard	1 (θ)	Logarithmic	Specialized
Atangana-Baleanu	1 (θ)	Exponential	Non-singular
ψ-Hilfer	2 (θ, κ) + $\psi(t)$	Flexible	Maximum

6.3. Comparison with machine learning approaches

In this work, the feedforward neural network serves exclusively as a post-processing validation tool to independently verify the numerical solutions obtained from the hybrid numerical scheme. It is not presented as a physics-informed learning framework nor as a primary methodological contribution. Table 5 compares our validation approach with existing machine learning methods for Lorenz systems.

Table 5. Comparison of existing approaches for Lorenz systems.

Method	Type	Frac.	Feature
DTSPC [21]	Synchronization diagnostic	No	Entropy-based complexity measure
VQLS [22]	Hybrid quantum	No	Variational quantum linear solver
RNN/LSTM [23]	Recurrent NN	Yes	Fractional-order time series prediction
Causal PINN+ResNet [24]	Physics-informed NN	No	Causal training + ResNet
Ours	Feedforward NN	Yes	Validation ($R^2 = 0.937$–0.983)

Abbreviations: DTSPC = Difference time series peak complexity; VQLS = Variational quantum linear solver; RNN/LSTM = Recurrent neural network/Long short-term memory; PINN = Physics-informed neural network.

Our contribution bridges traditional numerical methods [32] with machine learning by introducing neural network validation for the fractional-order Lorenz system. The high regression slopes (0.9407–0.9828) confirm topological equivalence [4], demonstrating that the neural network has successfully learned the underlying dynamics from our numerical data.

7. Conclusions and future work

This paper has analyzed the ψ-Hilfer fractional Lorenz system, whose memory and nonlocal effects offer flexible modeling of complex nonlinear problems. A qualitative study has established existence, uniqueness, and UH stability via fixed point theory. A novel hybrid numerical scheme has been developed, and solutions have been validated using a feedforward neural network (MSE: 1.085–5.186,

R^2: 0.937–0.983). Systematic investigation has revealed that decreasing fractional order θ enhances memory effects and stabilizes the system, while parameter κ modulates memory weight. A comparative analysis has been conducted against classical Lorenz systems, other fractional operators, and machine learning approaches. Simulations show that lower θ enhances mean-reversion and restrains volatility, implying greater persistence of past conditions. Thus, the ψ-Hilfer framework generalizes chaotic dynamics with memory, and neural network validation provides robust solution verification.

Based on these findings, future work includes: (i) complete bifurcation analysis to locate chaotic thresholds in θ and κ, complementing the Lyapunov estimates in Table 3; (ii) extension of the neural network validation to physics-informed architectures that embed the ψ-Hilfer operator directly; (iii) data-driven optimization of the auxiliary function $\psi(t)$ for specific applications; (iv) generalization of the present framework to higher-dimensional Lorenz-type and coupled fractional systems; and (v) exploration of a single coupled neural network with three inputs and three outputs to more naturally represent the fully coupled Lorenz system, in contrast to the three independent networks used in the present validation framework.

Author contributions

Ahmed Omar Alzahrani: Investigation, data curation, writing–review; Israr Ahmad: Methodology, writing–review, editing, writing–original draft; Ahmed Mohammed Alghamdi: Formal analysis, data curation, visualization; writing–review, editing, writing–original draft; Adel Aboud Bahaddad: Conceptualization, investigation; Khalid Ali Almarhabi: Software, supervision. All authors have read and approved the final version of the manuscript for publication.

Use of Generative-AI tools declaration

The authors declare they have not used Artificial Intelligence (AI) tools in the creation of this article.

Acknowledgments

This work was funded by the University of Jeddah, Jeddah, Saudi Arabia, under grant No. (UJ-25-DR-866). Therefore, the authors thank the University of Jeddah for its technical and financial support.

Conflict of interest

All authors declare no conflicts of interest in this paper.

References

1. J. Padilla, *Numerical validation of the discrete extramental clock law: Hierarchical emergence of objective time from ordinal conjunctions in chaotic systems*, Preprints, 2025.
2. K. M. Cuomo, A. V. Oppenheim, S. H. Strogatz, Synchronization of Lorenz-based chaotic circuits with applications to communications, *IEEE Trans. Circuits Syst. II Analog Digit. Signal Process.*, **40** (2002), 626–633. https://doi.org/10.1109/82.246163

3. D. Viswanath, S. Şahutoğlu, Complex singularities and the Lorenz attractor, *SIAM Rev.*, **52** (2010), 294–314. https://doi.org/10.1137/090753474
4. C. Letellier, L. A. Aguirre, Dynamical analysis of fractional-order Rössler and modified Lorenz systems, *Phys. Lett. A*, **377** (2013), 1707–1719. https://doi.org/10.1016/j.physleta.2013.05.006
5. I. Petráš, The fractional-order Lorenz-type systems: A review, *Fract. Calc. Appl. Anal.*, **25** (2022), 362–377. https://doi.org/10.1007/s13540-022-00016-4
6. S. Harikrishnan, O. Baghani, K. Kanagarajan, Qualitative analysis of fractional differential equations with ψ-Hilfer fractional derivative, *Comput. Methods Differ. Equ.*, **10** (2022), 1–11. https://doi.org/10.22034/cmde.2020.37370.1670
7. I. Mallah, I. Ahmed, A. Akgul, F. Jarad, S. Alha, On psi-Hilfer generalized proportional fractional operators, *AIMS Mathematics*, **7** (2021), 82–103. https://doi.org/10.3934/math.2022005
8. A. H. Bukhari, M. Shoaib, A. K. Kiani, N. I. Chaudhary, M. A. Z. Raja, et al., Dynamical analysis of nonlinear fractional order Lorenz system with a novel design of intelligent solution predictive radial base networks, *Math. Comput. Simul.*, **213** (2023), 324–347. https://doi.org/10.1016/j.matcom.2023.06.005
9. S. Taimur, M. A. Z. Raja, M. J. A. A. Raja, S. A. Hassan, S. Z. Abbasi, A. K. Kiani, et al., A hybrid intelligent computational framework for diverse firing patterns in a fractional-order locally active memristive neuron model, *Chaos Solit. Fract.*, **208** (2026), 118209. https://doi.org/10.1016/j.chaos.2026.118209
10. Z. Shah, M. A. Z. Raja, M. Shoaib, S. Javeed, T. Muhammad, M. Ali, et al., Computing intelligence for the magnetised chemically reactive bidirectional radiative nanofluid flow through the Bayesian regularisation back-propagated neural network, *Pramana*, **98** (2024), 130. https://doi.org/10.1007/s12043-024-02794-3
11. Z. Shah, M. A. Z. Raja, W. A. Khan, M. Shoaib, V. Tirth, A. Algahtani, et al., Computational intelligence paradigm with Levenberg-Marquardt networks for dynamics of Reynolds nanofluid model for Casson fluid flow, *Tribol. Int.*, **191** (2024), 109180. https://doi.org/10.1016/j.triboint.2023.109180
12. A. Akbar, H. Ullah, M. A. Z. Raja, K. S. Nisar, S. Islam, M. Shoaib, A design of neural networks to study MHD and heat transfer in two phase model of nano-fluid flow in the presence of thermal radiation, *Waves Random Complex Media*, **36** (2026), 157–180. https://doi.org/10.1080/17455030.2022.2152905
13. I. Ali, M. A. Z. Raja, C. Y. Chang, M. P. Khan, M. Shoaib, C. M. Shu, Machine learning knowledge-driven neuroarchitecture for analysis of three-dimensional boundary layer flow of Sisko nanofluid model with impact of magnetic field, *Z. Angew. Math. Mech.*, **106** (2026), e70350. https://doi.org/10.1002/zamm.70350
14. Z. I. Butt, I. Ahmad, M. A. Z. Raja, M. Shoaib, Radiative magneto-thermal modeling of tri hybrid nanofluid in blood: A Biomedical intelligent framework for hyperthermia cancer therapy, *J. Therm. Biol.*, **136** (2026), 104382. https://doi.org/10.1016/j.jtherbio.2026.104382
15. I. Grigorenko, E. Grigorenko, Chaotic dynamics of the fractional Lorenz system, *Phys. Rev. Lett.*, **91** (2003), 034101. https://doi.org/10.1103/PhysRevLett.91.034101

16. G. Li, X. Zhang, H. Yang, Numerical analysis, circuit simulation, and control synchronization of fractional-order unified chaotic system, *Mathematics*, **7** (2019), 1077. https://doi.org/10.3390/math7111077

17. D. Dai, X. Li, Z. Li, W. Zhang, Y. Wang, Numerical simulation of the fractional-order Lorenz chaotic systems with Caputo fractional derivative, *Comput. Model. Eng. Sci.*, **135** (2023), 1371–1392. https://doi.org/10.32604/cmes.2022.022323

18. Y. Wang, Z. Wei, G. Feng, Attractor radius for fractional Lorenz systems and their application to the quantification of predictability limits, *Chaos*, **33** (2023), 013105. https://doi.org/10.1063/5.0113709

19. K. M. Saad, M. S. Abdo, W. M. Hamanah, Existence and controllability analysis of multi-term fractional coupled systems with generalized-Caputo-Fabrizio operators, *Sci. Rep.*, **15** (2025), 34434. https://doi.org/10.1038/s41598-025-17523-y

20. M. Alqhtani, L. Sadek, Z. Hammouch, K. M. Saad, Efficient numerical schemes for linear fractional differential systems with applications to diffusion problems, *J. Franklin Inst.*, **362** (2025), 108144. https://doi.org/10.1016/j.jfranklin.2025.108144

21. Z. Lin, A. K. Pattanayak, A chaos synchronization diagnostic: Difference time series peak complexity (DTSPC), *Entropy*, **26** (2024), 1085. https://doi.org/10.3390/e26121085

22. S. F. Hafshejani, D. Gaur, A. Dasgupta, R. Benkoczi, N. R. Gosala, A. Iorio, A hybrid quantum solver for the Lorenz system, *Entropy*, **26** (2024), 1009. https://doi.org/10.3390/e26121009

23. A. E. Adeniji, K. S. Oyeleke, K. S. Ojo, A. M. Lasisi, Modeling and prediction of fractional-order chaotic Lorenz system using RNN and LSTM networks, *J. Niger. Assoc. Math. Phys.*, **69** (2025), 139–152. https://doi.org/10.60787/jnamp.vol69no1.487

24. M. H. Fan, J. H. Zhao, L. Ding, X. Y. Ma, R. L. Fu, Predicting nonlinear dynamic systems by causal physics-informed neural networks with ResNet blocks, *Neurocomputing*, **656** (2025), 131589. https://doi.org/10.1016/j.neucom.2025.131589

25. S. Scher, G. Messori, Generalization properties of feed-forward neural networks trained on Lorenz systems, *Nonlin. Processes. Geophys.*, **26** (2019), 381–399. https://doi.org/10.5194/npg-26-381-2019

26. X. Wang, J. Feng, Y. Xu, J. Kurths, Deep learning-based state prediction of the Lorenz system with control parameters, *Chaos*, **34** (2024), 033108. https://doi.org/10.1063/5.0187866

27. T. Abdeljawad, K. Shah, I. Ahmad, M. Hleili, M. S. Alatawi, Using a finite difference scheme together with neural networks analysis for propagation of the long waves equation, *AIMS Mathematics*, **11** (2026), 825–856. https://doi.org/10.3934/math.2026036

28. Asma, I. Ahmad, Z. Ali, S. Chasreechai, T. Sitthiwirattham, Analysis of a fractional order enzymatic reaction model with artificial neural network validation, *Eur. J. Pure Appl. Math.*, **18** (2025), 6923. https://doi.org/10.29020/nybg.ejpam.v18i4.6923

29. N. Vieira, M. M. Rodrigues, M. Ferreira, Fractional gradient methods via ψ-Hilfer derivative, *Fractal Fract.*, **7** (2023), 275. https://doi.org/10.3390/fractalfract7030275

30. I. Ahmad, Z. Ali, B. Khan, K. Shah, T. Abdeljawad, Exploring the dynamics of Gumboro-Salmonella co-infection with fractal fractional analysis, *Alex. Eng. J.*, **117** (2025), 472–489. https://doi.org/10.1016/j.aej.2024.12.119

31. E. Sousa, C. Li, A weighted finite difference method for the fractional diffusion equation based on the Riemann-Liouville derivative, *Appl. Numer. Math.*, **90** (2015), 22–37. https://doi.org/10.1016/j.apnum.2014.11.007

32. Q. Yang, C. Zeng, Chaos in fractional conjugate Lorenz system and its scaling attractors, *Commun. Nonlinear Sci. Numer. Simul.*, **15** (2010), 4041–4051. https://doi.org/10.1016/j.cnsns.2010.02.005

AIMS Press

© 2026 the Author(s), licensee AIMS Press. This is an open access article distributed under the terms of the Creative Commons Attribution License (http://creativecommons.org/licenses/by/4.0)